

Detectability of Transiting Jupiters and Low-Mass Eclipsing Binaries in Sparsely Sampled Pan-STARRS-1 Survey Data

Trent J. Dupuy¹ and Michael C. Liu^{1,2}

ABSTRACT

We present detailed simulations of the Pan-STARRS-1 (PS1) multi-epoch, multi-band 3π Survey in order to assess its potential yield of transiting planets and eclipsing binaries. This survey differs from dedicated transit surveys in that it will cover the entire Northern sky but provide only sparsely sampled light curves. Since most eclipses would be detected at only a single epoch, the 3π Survey will be most sensitive to deep eclipses ($\gtrsim 0.10$ mag) caused by Jupiters transiting M dwarfs and eclipsing stellar/substellar binaries. The survey will measure parallaxes for the $\sim 4 \times 10^5$ stars within 100 pc which will enable a volume-limited eclipse search, reducing the number of astrophysical false positives compared to previous magnitude-limited searches. Using the best available empirical data, we constructed a model of the extended solar neighborhood that includes stars, brown dwarfs, and a realistic binary population. We computed the yield of deeply eclipsing systems using both a semi-analytic and a full Monte Carlo approach. We examined statistical tests for detecting single-epoch eclipses in sparsely sampled data and assessed their vulnerability to false positives due to stellar variability. Assuming a short-period planet frequency of 0.5% for M dwarfs, our simulations predict that about a dozen transiting Jupiters around low-mass stars ($M_\star < 0.3 M_\odot$) within 100 pc are potentially detectable in the PS1 3π Survey, along with ~ 300 low-mass eclipsing binaries (both component masses $< 0.5 M_\odot$), including ~ 10 eclipsing field brown dwarfs. Extensive follow-up observations would be required to characterize these candidate eclipsing systems, thereby enabling comprehensive tests of structural models and novel insights into the planetary architecture of low-mass stars.

1. Introduction

Eclipsing systems are the gold standard by which theoretical models of stars, brown dwarfs, and extrasolar planets are tested, as they enable direct mass, radius, and temperature measurements. For example, mass and radius measurements of stars have provided critical tests of stellar interiors (Andersen 1991) and key insights into stellar magnetism (López-Morales 2007). In recent years, the discovery of transiting extrasolar planets has extended such fundamental measurements to the

¹Institute for Astronomy, University of Hawai'i, 2680 Woodlawn Drive, Honolulu, HI 96822

²Alfred P. Sloan Research Fellow

study of giant planets orbiting nearby stars (e.g., Charbonneau et al. 2000). The existence of such a population of short-period giant planets was originally a surprise, and the ongoing measurement of masses and radii for these planets continues to reveal remarkable diversity (Charbonneau et al. 2007, and references therein), spurring active research to characterize their atmospheres and understand their formation history.

The first multi-epoch all-sky surveys, such as Pan-STARRS (Kaiser et al. 2002), SkyMapper (Keller et al. 2007), and the planned Large Synoptic Survey Telescope (LSST; Tyson 2002), will soon open the door to the discovery of eclipsing systems different from those previously accessible. All-sky surveys contain the most comprehensive information for objects in the immediate solar neighborhood, which is populated predominately with M dwarfs. Historically, M dwarfs have been neglected by surveys for eclipsing binaries and transiting planets. This is because M dwarfs represent a tiny fraction of sources detected in magnitude-limited stellar variability surveys ($\sim 1:1000$, e.g., Shaw & López-Morales 2007). In addition, signal-to-noise (S/N) constraints have limited radial velocity (RV) searches for extrasolar planets to monitor only the nearest M dwarfs, which typically comprise $\sim 10\%$ of RV samples (e.g., Johnson et al. 2007). Consequently, there are only seven known eclipsing binaries with both component masses $< 0.5 M_{\odot}$ (Lacy 1977; Delfosse et al. 1999; Maceroni & Montalbán 2004; Creevey et al. 2005; Hebb et al. 2006; Blake et al. 2008b; Irwin et al. 2009a) and only one extrasolar planet known to transit an M dwarf (Gl 436b, Butler et al. 2004; Gillon et al. 2007).

Because of their small size ($0.1\text{--}0.5 R_{\odot}$), M dwarfs experience more extreme eclipses for a given size companion than solar-type stars. For example, the eclipse depth due to a transiting Jupiter-size object is $\sim 10\%$ for a mid-M dwarf ($\sim 0.3 R_{\odot}$), while it is an order of magnitude smaller ($\sim 1\%$) for a solar-type star. Such deep eclipses are in principle readily detectable in sparsely sampled light curves, where the interval between observing epochs is large compared to the periodic eclipse signal. The power of this approach has been demonstrated by the discovery of short-period M dwarf eclipsing binaries in both the Two Micron All Sky Survey (2MASS) calibration fields (Plavchan et al. 2008) and the SDSS-II Supernova Survey (Blake et al. 2008b).

Pan-STARRS-1 (PS1) is the first of the large, multi-epoch surveys to be on sky, having begun extensive on-sky commissioning runs in spring 2009. It will conduct a number of different surveys, including a conventional, dedicated transit survey pointed at a fixed position on the sky (Pan-Planets). We have instead focused on the 3π Survey (described in detail in Appendix A), the largest PS1 survey, which will image the entire 3π steradians of sky visible from Haleakala, on the island of Maui, at 12 epochs spanning 3 years in each of 5 bandpasses.¹ The cadence is designed to both detect asteroids and measure the parallaxes of nearby stars and is not specifically tailored to detect eclipsing binaries and transiting planets. However, its sparsely sampled light

¹The next largest PS1 survey is the Medium Deep Survey, which will image 10 PS1 fields (7 deg^2 each) at 72 epochs over 3 years in each of 5 bandpasses, with a ~ 4 -day cadence designed to detect supernovae. Since it covers only $\approx 0.2\%$ of the area of the 3π Survey, the Medium Deep Survey is a negligible source of nearby, low-mass eclipsing systems.

curves will be amenable to the detection of deep eclipses ($\gtrsim 0.10$ mag) such as those produced by eclipsing binaries or Jovian planets transiting M dwarfs. The light curves for the hundreds of thousands of low-mass stars in the immediate solar neighborhood with parallaxes measured by PS1 will enable a novel, volume-limited variability survey of the entire northern sky. Such an approach is conceptually similar to the MEarth Project (Nutzman & Charbonneau 2008; Irwin et al. 2009b), which is monitoring a carefully selected sample of 2000 nearby M dwarfs for planetary transits and has already discovered and characterized one eclipsing binary (Irwin et al. 2009a).

Previous transit surveys have been magnitude-limited and have thus encountered two challenges: (1) overcoming a broad range of astrophysical false positives that mimic planetary transits and are more numerous by $\sim 20:1$ (e.g., Bouchy et al. 2005; Pont et al. 2005; O’Donovan et al. 2006); (2) obtaining follow-up observations on transit host stars that are fainter than those discovered by dedicated RV surveys. A volume-limited sample naturally reduces such rare astrophysical false positives and focuses on only the nearest, and thus brightest, stars in the sky. Also, even if no events are detected, such a well-defined sample can enable meaningful statements about the underlying population of eclipsing systems, which can be challenging to quantify for magnitude-limited samples. However, sparsely sampled light curves are potentially more vulnerable to mundane false positives (e.g., due to star spots or photometric outliers) since by definition they contain no information about the light curve shape during eclipse.

Previous authors have estimated the transit yield of Pan-STARRS, considering all stars detected within the magnitude limits of selected surveys. Gaudi (2007) and Beatty & Gaudi (2008) used analytic relations to derive the number of transits for solar-type stars (~ 20) and M dwarfs (~ 40) in the magnitude-limited sample of the PS1 Medium Deep Survey. Ford et al. (2008) used a semi-analytic approach and, assuming that a large fraction (10%) of M dwarfs host a short-period ($1 < P < 3$ days) Neptune-mass planet, estimated that ~ 300 transits in the 3π Survey and ~ 10 transits in the Medium Deep Survey could be detected. Neither of these results are directly comparable to our simulations, as we have used substantially different input assumptions, most importantly restricting ourselves to a volume-limited sample, and we also evaluate the detectability of such events in simulated survey light curves. In addition, we consider low-mass eclipsing binaries, which produce essentially the same eclipse signal in the sparsely sampled light curves as Jupiters transiting M dwarfs. Such “false positives” in the search for planets would be interesting in their own right, given the small number of low-mass eclipsing binaries currently known.

In this paper, we predict the yield of eclipsing binaries and transiting Jupiters in PS1 3π Survey data. Using the best available empirical information, we have constructed a model of the solar neighborhood encompassing solar-type stars to the coldest known brown dwarfs, including a realistic binary population. We have developed a method for analytically predicting the planetary transit yield given an inventory of survey targets. We also constructed Monte Carlo simulations to predict the yield of both planets and eclipsing binaries and to characterize their host stars, while carefully considering the false positive rate due to star spots. The prospects of characterizing the candidate eclipsing systems found in sparsely sampled light curves with follow-up observations is discussed in

detail, along with the impact of our input assumptions on the survey yield.

2. Model of the Solar Neighborhood

We first created a model that describes the population of stellar and substellar objects within the solar neighborhood. These are the host stars for the transiting/eclipsing systems. The distance limit is set by the astrometric precision of the survey, since this determines the smallest parallaxes it will be able to measure. Both PS1 and LSST have astrometric precision goals of 10 mas per epoch, which will enable $S/N > 10$ parallax measurements for objects within 100 pc. Since this distance is smaller than the scale length and height of the Galactic disk (2600 pc and 300 pc; Jurić et al. 2008), we assumed that objects are uniformly distributed within this volume.

We assigned the properties of these simulated objects as follows: (1) masses and ages were drawn from appropriate initial mass and birth rate functions; (2) luminosities and radii were determined from evolutionary models; (3) spectral types were assigned based on an empirical relation with luminosity, (4) optical and near-infrared colors and bolometric corrections were assigned based on empirical relations with spectral type; (5) binary companions were assigned to an appropriate fraction of simulated objects, with the orbital separations and mass ratios randomly drawn from empirical distributions; and (6) short-period ($P < 11.5$ days) Jupiter-like planets were assigned to an appropriate fraction of simulated objects, with orbital periods randomly drawn from an empirical distribution.

The resulting population of low-mass stars ($M < 1.0 M_{\odot}$) and brown dwarfs is summarized in Table 1. We list both the total number of objects within 100 pc (over 4π steradians) and the objects expected to be within the magnitude limits and areal coverage of the PS1 3π Survey, which is described in Appendix A. For example, our model predicts that a total of 94 M dwarfs within 100 pc host planets with orbits aligned such that transits are observable from Earth. Of the 70 of these in the 3π steradians observable by PS1, 56 are expected to be within the magnitude limits of the 3π Survey (14 are saturated). In our simulations, the number of actual transits observed by PS1 will be some subset of these 56, depending on if transit events occur at the observation epochs.

2.1. Low-mass Stars and Brown Dwarfs

As the starting point for our simulation, we drew masses and ages of objects from appropriate random distributions. For ages, we assumed a constant star formation rate over a period of 10 Gyr (e.g., Gizis et al. 2002; Robin et al. 2003). For the mass function, we used the best fit log-normal function derived by Covey et al. (2008). The number of objects in our simulation was determined by the normalization of this mass function ($0.1 \log(M/M_{\odot})^{-1} \text{ pc}^{-3}$), which predicts that there are 4.0×10^5 objects within 100 pc.

To determine the physical properties of the simulated objects, we used solar-metallicity Lyon evolutionary models (Baraffe et al. 1998; Chabrier et al. 2000; Baraffe et al. 2003) to derive luminosities and radii. We created a 2-dimensional array, uniformly gridded in $\log M$ and $\log(\text{age})$, for each model-predicted property. Then, for each simulated object, we bilinearly interpolated its model-predicted $\log L_{\text{bol}}$ and $\log R$ from these arrays. Because our simulated objects span a wide range of masses and temperatures (from low-mass main-sequence stars to old brown dwarfs), different evolutionary models are appropriate for different simulated objects. We used the models of Baraffe et al. (1998) for objects where these models predicted an effective temperature > 2800 K, i.e., too hot to harbor appreciable amounts of dust in the atmosphere (e.g., Tsuji et al. 1996; Jones & Tsuji 1997). We used the DUSTY models of Chabrier et al. (2000) for objects where these models predicted effective temperatures > 1400 K and the COND models of Baraffe et al. (2003) for the remaining objects. This break in temperature roughly corresponds to the transition from L to T dwarfs (e.g., Golimowski et al. 2004; Dupuy et al. 2009b), where dust clouds sediment below the photosphere.

We assigned spectral types to the simulated objects based on their model-predicted luminosities. We compiled the luminosities derived by Leggett et al. (2000, 2002) and Golimowski et al. (2004) for M, L, and T dwarfs with measured distances and spectral energy distributions. We were careful to exclude known and suspected binaries from this sample (Liu et al. 2006). This resulted in 63 objects ranging in spectral type from M1 to T8, adopting near-infrared spectral types when possible. We supplemented this sample with luminosities for the spectral types G0, G2, K0, K2, K5, and M0 tabulated by Cox (2000), and originating from Schmidt-Kaler (1982) and de Jager & Nieuwenhuijzen (1987). In order to assign spectral types to simulated objects, we derived a polynomial relation between spectral type (SpT)² and L_{bol} , which is shown in Figure 1 with the polynomial coefficients given in Table 2.

The last remaining property that we determined for simulated objects were their absolute magnitudes in the relevant optical and near-infrared bandpasses. We chose not to use the absolute magnitudes predicted by evolutionary models because it is well known that they do not accurately reproduce the colors of very low-mass stars and brown dwarfs (e.g., Dupuy et al. 2009a,b). Instead we used K -band bolometric corrections (BC_K) combined with observed optical and near-infrared colors. Leggett et al. (2000, 2002) and Golimowski et al. (2004) derived BC_K values for all 63 M, L, and T dwarfs with measured luminosities. We again supplemented this sample with tabulated values from Cox (2000), which are based on V -band bolometric corrections from Johnson (1966) and $V - K$ colors from Bessell & Brett (1988) and Bessell (1991). We fit a polynomial relation between BC_K and SpT in order to determine bolometric corrections, and thus absolute magnitudes in K -band, for simulated objects. The fit is shown in Figure 1, and the coefficients are given in Table 2.

²In assigning numerical spectral types, we assumed each spectral class comprised 10 subclasses, even though this is not always formally correct (e.g., for the K spectral class).

To determine the optical and near-infrared colors of the low-mass stars in our simulation, we compiled existing photometry and also computed colors from synthetic photometry of publicly available spectra (Appendix A). To properly account for the observed intrinsic scatter in color at each integer spectral type, we drew colors from Gaussian distributions with the observed mean and root-mean-squared (rms). For M0–L0 dwarfs, we used the tabulated mean and rms $g-r$ colors from Bochanski et al. (2007) and the tabulated mean and rms $r-i$, $i-z$, $z-J$, and $J-K$ colors from West et al. (2008).³ For L1–T8 dwarfs, we used the $r-i$, $i-z$, and $z-J$ colors of the 196 objects from Hawley et al. (2002), Knapp et al. (2004), and Chiu et al. (2006), after excluding objects known or suspected to be binaries. In Appendix A, we have derived conversions between the SDSS and PS1 photometric systems, which we applied to this SDSS photometry.⁴ For the $J-K$ colors of L1–T8 dwarfs, we used the tabulated mean and rms values of Faherty et al. (2009), converting these 2MASS colors to the MKO photometric system using the relations of Stephens & Leggett (2004). For G0–K7 dwarfs, we used the Pickles (1998) library of averaged stellar spectra to derive colors from synthetic photometry, adopting 0.10 mag for the intrinsic rms scatter at these spectral types. Finally, because the y bandpass for PS1 is unique, we derived $y-J$ colors solely from synthetic photometry of the publicly available spectra described in Appendix A. The compiled and derived colors are shown as a function of spectral type in Figure 2 and Table 3. We required a minimum of 2 objects at a given spectral type to compute the mean, and 3 objects to compute the rms. Where the mean or rms was not available for a given spectral type, we interpolated its value from the neighboring spectral type bins.

2.2. Binary Companions

We used the results of multiplicity studies targeting specific mass/spectral type intervals of low-mass stars and brown dwarfs to assign binary companions to simulated objects.

For objects with masses $> 0.5 M_{\odot}$ (i.e., FGK dwarfs), we adopted the results of Duquennoy & Mayor (1991, DM91 hereinafter). We drew mass ratios ($q \equiv M_2/M_1$) according to the DM91 cumulative distribution for $P < 10^4$ day binaries corrected for viewing angle effects and completeness (i.e., line 3 of their Table 7).⁵ This cumulative distribution and the resulting mass ratio distribution are shown in Figure 3. We drew periods from a log-normal distribution with a

³No g -band photometry or spectroscopy is available for spectral types later than L0, so we cannot assign $g-r$ colors beyond L0, implicitly assuming they will be undetectable in g -band for the purposes of this simulation.

⁴Since there are no SDSS measurements in g and r band for later spectral type objects than we have derived photometric conversions for ($> M6$ in g , $> L5$ in r), we simply use the conversion at the most extreme spectral type for which it is defined at all later spectral types. This affects very few objects as such faint, red objects are not typically detected in the bluest bandpasses.

⁵We caution that the lowest mass ratio bins of DM91 ($q < 0.2$) depend strongly on their assumed completeness corrections as they were not sensitive to very low-mass companions. However, this has no impact on our results as we found that all $> 0.5 M_{\odot}$ stars within 100 pc are saturated in the PS1 3π Survey.

mean of $\log(P/\text{days}) = 4.8$ and $\sigma_{\log P} = 2.3$ and used the system mass $M(1 + q)$ to convert the orbital period to semimajor axis (a). We assigned companions to 57% of $M > 0.5 M_{\odot}$ objects, in accordance with the binary frequency found by DM91.

For objects with masses $0.1 < M < 0.5 M_{\odot}$ (roughly M0–M6 dwarfs), we adopted the results of Fischer & Marcy (1992, FM92 hereinafter). They found a log-normal distribution of orbital periods consistent with that of DM91, which implies somewhat more compact orbits than for FGK dwarf binaries at a given period according to Kepler’s Third Law ($a \propto M^{1/3}$). We drew mass ratios from the cumulative distribution of the entire sample of FM92 (their Table 1). This cumulative distribution and the resulting mass ratio distribution are shown in Figure 3. Companions were assigned to 42% of simulated objects in this mass range, in accordance with the binary frequency found by FM92.

The binary properties of very low-mass stars and brown dwarfs ($M < 0.1 M_{\odot}$) are less well constrained by observations than for FGKM dwarfs. However, two attributes of very low-mass binaries have become clear from previous multiplicity studies: (1) binaries with separations wider than $\gtrsim 15$ AU are rare (e.g., Close et al. 2003) and (2) mass ratios are rarely very different from unity (e.g., Burgasser et al. 2007). From a uniform analysis of the results from high-resolution imaging surveys targeting $> M6$ dwarfs, Allen (2007) found that the mass ratio distribution of binaries was adequately described by a power law ($dN/dq = q^{-\gamma}$), where $\gamma = -1.8 \pm 0.6$.⁶ We used this power law to draw the mass ratios of companions, and the resulting distribution is shown in Figure 3. Imaging surveys have been able to constrain the distribution of orbital separations outside of ~ 2 AU, and Close et al. (2003) found that 15% of $> M8$ dwarfs have companions at wider separations than this. Accounting for the detection limits of existing surveys, Allen (2007) suggested an additional $\sim 5\%$ of objects have undetected companions with separations $\gtrsim 1$ AU. The only existing surveys sensitive to the much tighter separations relevant to eclipsing systems are RV surveys (e.g., Guenther & Wuchterl 2003; Joergens 2006; Basri & Reiners 2006). Maxted & Jeffries (2005) found that a significant fraction of objects (an additional 20–30%) may harbor close companions, given four spectroscopic binaries identified in RV surveys. Basri & Reiners (2006) contributed additional radial velocity data and, using a slightly different analysis, found that the fraction of objects hiding close companions is $11^{+7}_{-4}\%$. In fact, they found that a log-normal period distribution could reasonably explain the ensemble of data if the distribution was truncated at 15 AU. We drew orbital periods from this truncated log-normal distribution, with a peak at $\log(P/\text{days}) = 3.8$ and $\sigma_{\log P} = 1.3$. Companions were assigned to 26% (i.e., 15 + 11%) of $M < 0.1 M_{\odot}$ objects.

⁶This is somewhat at odds with the power-law slope of $\gamma = -4.2 \pm 1.0$ derived by Burgasser et al. (2007) for L and T dwarfs. Allen (2007) suggests that this is due to a steepening of the power law at lower masses, since the Burgasser et al. (2007) sample focuses on lower mass objects. Regardless, the mass ratio distribution has a negligible effect on our primary result (i.e., the survey yield of eclipsing systems) since for very low-mass stars and brown dwarfs the mass–radius relation is essentially flat.

The physical and observational properties of the companions were determined in the same manner as described for single stars in Section 2.1. Companions falling outside the luminosity range of G0–T8 dwarfs were excluded from the simulation, and for the remaining companions we included their flux when considering survey detectability. The short-period tail of the log-normal distributions we used to assign companions resulted in some systems that would be non-detached binaries. Since we are interested in detached eclipsing systems, we excluded binary companions where the radius of the primary intruded into the companion’s Hill sphere ($R_1 > a(1 - (\frac{M_2}{3M_1})^{1/3})$).

2.3. Short-period Jupiters

For solar-type host stars, the population of Jupiter-like planets in short-period orbits is very well characterized, despite their rarity, thanks to long-term radial velocity observing programs that have targeted thousands of stars. In a recent analysis of the Keck Planet Search, Cumming et al. (2008) found that $1.1 \pm 0.5\%$ of targets have a massive planet ($M \sin i > 0.5 M_{\text{Jup}}$) in a short-period orbit ($P < 11.5$ days).⁷

Fewer planets are known around M dwarfs, so their population of short-period planets is not as well characterized. Only one transiting planet around an M dwarf is known (Gl 436b, Gillon et al. 2007), with a mass of $0.072 M_{\text{Jup}}$ and radius of $0.44 R_{\text{Jup}}$ (Torres 2007). Like many of the other known planets around M dwarfs, Gl 436b is much less massive than Jupiter and more akin to Neptune in its mass and radius. Johnson et al. (2007) used the California and Carnegie Planet Search detections of giant planets ($M \sin i > 0.8 M_{\text{Jup}}$) within 2.5 AU to derive a giant planet fraction of $4.2 \pm 0.7\%$ for FGK stars ($0.7 < M_\star < 1.3 M_\odot$) and $1.8 \pm 1.0\%$ for late-K and M dwarfs ($M_\star < 0.7 M_\odot$). We adopt the ratio of these planet fractions as the relative rate of occurrence of planets around M dwarfs compared to solar-type stars. Thus, if 1.1% of solar-type stars have short-period Jupiters (Cumming et al. 2008), then 0.47% of M dwarfs are assumed to have such planets.

We assigned a short-period planet to 0.47% of simulated objects with $M_\star < 0.7 M_\odot$ and to 1.1% of simulated objects with $M_\star > 0.7 M_\odot$. We drew orbital periods from the cumulative distribution of all short-period planets ($P < 11.5$ days) in the Catalog of Nearby Exoplanets (Butler et al. 2006).⁸ The median orbital period was 3.8 days, and the mean and rms were 4.5 ± 2.3 days. We assumed a single radius of $1.0 R_{\text{Jup}}$ for all planets and that the planets contributed no flux to the system. We also assumed circular orbits, as short-period orbits are expected to be tidally circularized, and neglected the mass of the planet when converting the orbital period to semimajor

⁷As discussed in Section 2.2 of Beatty & Gaudi (2008), the bias of RV surveys toward metal-rich stars may result in an overestimation of the planet frequency by as much as a factor of ~ 2 , in comparison to a volume-limited sample.

⁸<http://exoplanets.org/planets.shtml>

axis.

3. Survey Yield Predictions

We have taken two approaches to simulating the yield of transit events in sparsely sampled multi-epoch survey data: (1) a semi-analytic approach which assigns transit detection probabilities to individual survey stars and (2) a full Monte Carlo simulation in which light curves for all survey stars are generated and searched for transit events. In both cases, we assume that survey light curves will be randomly sampled in phase, neglecting any window function effects. This assumption is valid for surveys in which the typical interval between observation epochs is much longer than that of the periodic signal being sought.

Sparsely sampled light curves require a different approach to eclipse detection than is used for the densely sampled light curves from conventional transit surveys. The most important difference is that transits are expected to only be detected at a single epoch. Appendix B describes the eclipse detection algorithms we have considered. For the simulations described below, we used a “S/N model” (algorithm 3 in Appendix B) to assess the transit yield. Our results do not depend strongly on the algorithm used because they all have comparable detection sensitivities. For real data, the best algorithm will depend on the number of light curve points (Figure 11) and the dominant source of false positives (Figure 12).

3.1. Semi-analytic Calculation

We first consider an analytic method to assign transit detection probabilities to survey stars. The following approach to computing the survey yield is only semi-analytic because it uses as a starting point the Monte Carlo simulation of the solar neighborhood described in Section 2. However, given real survey data for a well-characterized set of target stars this approach could be used to compute the expected transit yield directly, given assumptions about the underlying planet population.

The concept behind this approach is that each survey star has some minimum detectable fractional eclipse depth (δ_{\min}), given the photometric S/N of the star (S/N_{\star}), the total number of points in its light curve (n), the number of points in which the transit was observed (n_{obs}), and the transit S/N threshold (S/N_{\min}). We consider two cases, one in which the photometric S/N of the star is photon-limited and improves as \sqrt{n} , and one in which it is at the systematic noise floor (S/N_{floor}), which for PS1 is expected to be about 100 (i.e., $\sigma_{\text{floor}}/N_{\star} = 1\%$). To derive δ_{\min} , we

first use Equation B3 to find how the transit S/N depends on the fractional eclipse depth (δ):

$$S/N_{\text{transit}} = \begin{cases} \frac{N_{\star} \delta}{\sqrt{\frac{N_{\star}}{n-n_{\text{obs}}} + \frac{N_{\star}(1-\delta)}{n_{\text{obs}}}}} = \frac{S/N_{\star} \delta}{\sqrt{\frac{1}{n-n_{\text{obs}}} + \frac{1-\delta}{n_{\text{obs}}}}} & \text{if } S/N_{\star} < S/N_{\text{floor}} \\ \frac{N_{\star} \delta}{\sqrt{N_{\star}^2 \sigma_{\text{floor}}^2 + N_{\star}^2 (1-\delta)^2 \sigma_{\text{floor}}^2}} = \frac{S/N_{\star} \delta}{\sqrt{1+(1-\delta)^2}} & \text{if } S/N_{\star} = S/N_{\text{floor}} \end{cases} \quad (1)$$

We can then solve for the eclipse depth corresponding to the transit detection threshold (S/N_{min}):

$$\delta_{\text{min}} = \begin{cases} \frac{(S/N_{\text{min}})^2}{2n_{\text{obs}}(S/N_{\star})^2} \left[\sqrt{1 + \frac{4(S/N_{\star})^2}{(S/N_{\text{min}})^2} \left(\frac{n_{\text{obs}}^2}{n-n_{\text{obs}}} + n_{\text{obs}} \right)} - 1 \right] & \text{if } S/N_{\star} < S/N_{\text{floor}} \\ \left(1 - \frac{(S/N_{\star})^2}{(S/N_{\text{min}})^2} \right)^{-1} \left[1 - \sqrt{1 - 2 \left(1 - \frac{(S/N_{\star})^2}{(S/N_{\text{min}})^2} \right)} \right] & \text{if } S/N_{\star} = S/N_{\text{floor}} \end{cases} \quad (2)$$

In the case where $S/N_{\star} = S/N_{\text{floor}}$, there is no dependence on the number of light curve points because the photometric error is not improved by adding more measurements. For a given set of orbital parameters and planet radius, the fraction of the orbital period during which the flux diminution exceeds this threshold is proportional to the probability of observing that transit. By appropriately averaging over all orbital phases and inclinations a detection probability can be computed for each star.

The eclipse depth (δ) for a uniformly illuminated stellar disk is a function of the projected separation between the planet and star (z , which is in units of R_{\star}) and the ratio of their radii ($p \equiv R_{\text{p}}/R_{\star}$)

$$\delta = \begin{cases} 0 & z \geq 1 + p \\ \frac{1}{\pi} \left[p^2 \kappa_0 + \kappa_1 - \sqrt{\frac{4z^2 - (1+z^2-p^2)^2}{4}} \right] & |1-p| < z < 1+p \\ p^2 & z \leq 1-p \\ 1 & z \leq p-1 \end{cases} \quad (3)$$

where $\kappa_0 = \cos^{-1}[(p^2 + z^2 - 1)/2pz]$ and $\kappa_1 = \cos^{-1}[(1 - p^2 + z^2)/2z]$ (Mandel & Agol 2002). The projected separation between the planet and star (z) is a function of the orbital elements and phase

$$z = \frac{a \sqrt{1 - \sin^2 i \cos^2 \theta}}{R_{\star}} \left(\frac{1 - e^2}{1 - e \sin(\theta - \omega)} \right) \quad (4)$$

where e is the eccentricity, ω is the argument of periastron, θ is the orbital phase, and i is the inclination (Gimenez & Garcia-Pelayo 1983). Since we assumed circular orbits, the rightmost term that depends on eccentricity becomes unity.

For a given inclination, the probability of observing a transit is the fraction of the orbital period during which $\delta > \delta_{\text{min}}$. It is impossible to compute this directly because, by inspection of Equations 3 and 4, the relevant equations are transcendental; therefore, we computed this numerically. First, we reduced the problem to three independent variables in dimensionless form: δ_{min} ,

R_\star/a , and R_p/R_\star . For a given inclination, these variables uniquely specify the range of orbital phase over which $\delta > \delta_{\min}$, and we refer to this interval of phase as $\Delta\theta_{\text{obs}}$. To compute the probability of observing a transit (P_{obs}), we numerically integrated these phase intervals as a function of inclination, weighting by the inclination probability distribution

$$P_{\text{obs}} = \int_0^{\pi/2} \frac{\Delta\theta_{\text{obs}}(i)}{2\pi} \cos i \, di \quad (5)$$

Because this is computationally intensive, we created a look-up cube for the value of P_{obs} as a function of the three independent variables (δ_{\min} , R_\star/a , and R_p/R_\star) and trilinearly interpolated this cube to assign probabilities to the stars in our simulation. Since P_{obs} accounts for both the transit viewing angle probability (R_\star/a) and chance of catching the transit at some moment in time ($\approx R_\star/\pi a$), it scales roughly as $(R_\star/a)^2$. Of course, P_{obs} can be significantly smaller than this if the minimum detectable depth (δ_{\min}) only allows a fraction of the transit to be detectable.

Finally, to determine the probability (P_{det}) that a transit would actually be detected in the survey, we used the binomial distribution

$$P_{\text{det}} = \frac{n!}{n_{\text{obs}}!(n - n_{\text{obs}})!} P_{\text{obs}}^{n_{\text{obs}}} (1 - P_{\text{obs}})^{n - n_{\text{obs}}} \quad (6)$$

where n is the total number of light curve points and n_{obs} is the number of points in which the transit was observed. For the sparsely sampled light curves that we considered, we assumed that transits are only ever observed once by the survey ($n_{\text{obs}} = 1$), and thus $P_{\text{det}} \approx nP_{\text{obs}}$ since P_{obs} is small. The assumption that $n_{\text{obs}} = 1$ is valid because PS1 will spend a total of only 6–12 minutes per bandpass over the 3-year 3π Survey observing each star, which is a small fraction of the typical orbital period (median 3.8 days). To calculate the survey yield of detected transits, we simply summed the values of P_{det} determined for all the stars with assigned planets. The results are given in Table 4, where we have used a threshold of $S/N > 7$ (see Section 3.2). We found that about 16 transits are detectable in the PS1 3π Survey, with a slight preference to be detected in g , r , and y bands as fewer nearby M dwarfs are saturated in these bands compared to i and z . We have conservatively treated light curves from different bandpasses separately (n.b., observations in different bandpasses are *not* observed simultaneously in PS1, unlike SDSS). However, it may be possible to combine data from different bandpasses to enable more robust rejection of false positives.

3.2. Monte Carlo Simulation

While the semi-analytic approach allows a direct computation of the transit yield, its limitations motivated us to perform a full Monte Carlo simulation of survey light curves. One limitation is that we implicitly assumed that the planet contributes no flux to the light curve in the semi-analytic approach. Thus, without adding more parameters it cannot be used to predict the survey yield of eclipsing binaries, where the flux diminution during transit is reduced by the light from a companion. In the semi-analytic approach we also could not assess potential sources of false

positives, the effects of stellar limb-darkening, or how often systems are observed in eclipse more than once.

In our Monte Carlo simulations, light curves were randomly drawn for every survey star. The flux of each star was determined from its magnitude in the PS1 bandpasses and the zero points derived in Appendix A. Poisson noise was added to the light curves, accounting for the flux diminution due to any eclipses. Eclipse light curves were generated using the publicly available routines of Mandel & Agol (2002),⁹ assuming either a uniformly illuminated stellar disk or a quadratic limb-darkening law. We drew random orbital inclinations, and planet and binary parameters were drawn from the distributions described in Sections 2.2 and 2.3. Limb-darkening coefficients for the PS1 bandpasses were bilinearly interpolated from the models of Claret (2004) for the SDSS filters, which are tabulated in T_{eff} and $\log(g)$. As shown in Appendix A (Figure 8), the SDSS and PS1 *griz* bandpasses are similar, and for the PS1 *y*-band we used the SDSS *z*-band limb-darkening coefficients.

In order to assess eclipse false positives due to star spots, we added sinusoidal variability to a fraction of the light curves. Since M dwarfs are the primary source of detected eclipsing systems and can potentially have large amplitude variability due to spots, we only added simulated variability to M dwarfs. We used the best available information on such periodic variability from Rockenfeller et al. (2006), who found a median variability amplitude of 0.014 mag (0.005–0.02 mag observed range) in their *G*, *R*, and *I* bands for $21 \pm 11\%$ of M dwarfs. In Appendix B, we discuss the issue of false positives in more detail, considering other cases beyond our simple M dwarf spot model.

We ran separate simulations for planets and binary companions (i.e., we did not consider transiting planets in double star systems) and we used the “S/N model” (algorithm 3 in Appendix B) in a blind search of the simulated light curves for eclipse events. The results are shown in Table 4, where we have again treated bandpasses separately, as in our semi-analytic approach. We adopted a threshold of $S/N > 7$ in order to make the number of false positives vanishingly small.¹⁰ Summing the detections in individual bandpasses, the survey yield for planets is in good agreement with the results from the semi-analytic approach (both find 16 transits). We also found that limb-darkened eclipse curves gave the same numbers to within $\sim 10\%$ as uniform disk illumination, and thus in Table 4 we only quote the uniform disk results as these are directly comparable to the semi-analytic results.

For the PS1 3π Survey, the Monte Carlo simulations predict that about 16 transits for 13 Jupiters orbiting M dwarfs are detectable, so about three transits are detected in two different bandpasses over the course of the survey. However, the vast majority of detected flux dips are

⁹<http://www.astro.washington.edu/users/agol/transit.tar.gz>

¹⁰Note that if our choice of $S/N > 7$ is an unrealistically optimistic threshold, this does not sensitively impact the planet or eclipsing binary yield. Figures 6 and 7 show that the median S/N of detected transits and eclipses are about 15 and 20, respectively.

predicted to be due to eclipsing binaries: 570 eclipses for 260 eclipsing binaries. About 40% of these binaries are detected in only one bandpass, about 25% are detected in two, and about 15%/10%/10% are detected in 3/4/5 bands. Because different bandpasses are not observed simultaneously, such multi-band detections cannot be used to measure the color in and out of eclipse, which could help distinguish planets from stellar companions.

Figure 6 shows that the host stars of detected transiting Jupiters are overwhelmingly mid-M dwarfs (M3–M5), which is not surprising as these are the most common stars in a volume-limited sample (Reid et al. 2004). Figure 7 shows that the primary stars of detected eclipsing binaries are also predominantly mid-M dwarfs, and the secondaries range from mid-M to L and T dwarfs. Our simulations predict ~ 10 eclipsing binaries with a substellar secondary, and these would be important discoveries as there are currently no known field brown dwarfs in eclipsing binaries and therefore no direct measurements of the radii of brown dwarfs.

Different bandpasses contribute different numbers of eclipsing binaries by a factor of ~ 2 . For example, the g band contributes about twice as many eclipses as the i or z bands. This is a natural consequence of the fact that M dwarfs have red optical colors and the detection volume of mid-M dwarfs within 100 pc is most strongly limited by saturation. Thus, the effective volume of g band is ~ 2 larger than i or z bands because saturation affects g band less (see Figure 10 in Appendix A).

4. Discussion

Our simulations have shown that a large population of eclipsing binaries, in which mid-M dwarfs are the primary star, are likely to be detected by multi-epoch all-sky surveys such as the PS1 3π Survey. Given reasonable assumptions for the planet fraction, we also predict that a substantial number of transiting Jupiters may be detectable, also around mid-M host stars. We now discuss how our results are impacted by the input assumptions to our simulations, as well as the prospects for confirming candidate eclipsing systems using follow-up observations.

4.1. Impact of Assumptions on Survey Yield

- *M dwarf planet frequency.* The transit yield depends directly on the assumed planet frequency. Currently, no M dwarfs are known to host a transiting Jupiter-mass planet, so this fraction is very uncertain. Several M dwarfs are known to host planets, about half of which are less massive than Neptune (Bailey et al. 2009). Such a preference of lower mass stars to form lower mass planets was predicted by Laughlin et al. (2004), and subsequent models (Ida & Lin 2005; Kennedy & Kenyon 2008) now also reproduce the observational result of

Johnson et al. (2007) that Jupiter-mass planets are less common around lower mass stars.¹¹ Some fraction of M dwarfs do form Jupiter-mass planets, and there are currently several examples of such systems discovered by RV and microlensing surveys (Delfosse et al. 1998a; Marcy et al. 1998; Butler et al. 2004; Johnson et al. 2007; Bailey et al. 2009; Dong et al. 2009). We have simply scaled the fraction of short-period Jupiters from solar-type host stars (1.1%) to M dwarfs (0.47%) using the relative Jupiter-mass planet fraction found by Johnson et al. (2007). However, due to the uncertainty in the different formation and migration histories of planets orbiting solar-type stars and M dwarfs, this assumption may not be correct. Ultimately, our findings suggest that the PS1 3π Survey will be capable of addressing this question since it would find $\gtrsim 10$ transiting Jupiters if this simple scaling is correct and $\gtrsim 20$ if the population were identical to solar-type stars. Thus, even a null result would place meaningful upper limits on the population of short-period Jupiters around M dwarfs.

- *M dwarf planet orbital parameters.* Our assumptions about the orbital parameters of short-period Jupiters around M dwarfs also affect the transit yield. We have assumed a period distribution identical to that of all observed short-period planets, which is dominated by the planetary systems of solar-type stars. The short period “pile-up” in the planet period distribution is commonly attributed to the halting of planetary migration because of an inner edge to the circumstellar disk (e.g., Kuchner & Lecar 2002). Thus, M dwarfs may have a systematically different period at which planets terminate their migration. Given their lower energy output, the inner disk edge for M dwarfs should be closer to the star, which would result in a shorter pile-up period and an increase in the number of detected transits. For example, if the inner disk edge occurs at a fixed temperature, where the gas becomes ionized (Stone et al. 2000) and/or dust sublimates (Sano et al. 2000), its distance from the star will scale as $a \propto \sqrt{L_\star}$. During pre-main-sequence evolution $L_\star \propto M_\star^2$ (Siess et al. 2000), so the location of the inner disk edge is expected to scale as $a \propto M_\star$ and the orbital period as $P \propto \sqrt{a^3/M_\star} \propto M_\star$. Short-period planets around solar-type stars ($P < 11.5$ days, $0.7 < M_\star < 1.3 M_\odot$) in the Catalog of Nearby Exoplanets (Butler et al. 2006) have a median orbital period of 3.9 days, thus such planets around mid-M dwarfs ($0.3 M_\odot$) would be expected to have a median orbital period of 1.3 days. This would drastically change the predicted number of detectable transiting planets in our simulations. We ran a simulation in which we assumed orbital periods scaled with mass for all M dwarfs, and the number of predicted transit detections increased by a factor of ~ 4 .

We have also assumed an eccentricity of zero for planets, as well as eclipsing binaries, which is expected from tidal circularization of such short-period orbits (e.g., Zahn 1977). However, if the orbits possessed modest eccentricities such as those observed for longer period planets ($P > 10$ days, median eccentricity of 0.3), Burke (2008) has shown that this would result in

¹¹Such models typically rely on a correlation between the stellar mass and protoplanetary disk mass ($M_{\text{disk}} \propto M_\star$). However, observations of circumstellar disks show no such correlation (e.g., Andrews & Williams 2005), and models that do not include this correlation find that planets are *more* common around lower mass stars (Kornet et al. 2006).

a 25% increase in transit probability.

- *Mass function.* Both the eclipsing binary and transit yield depend strongly on the functional form and overall normalization of the mass function, as these determine the proportion of M dwarfs and total number of stars, respectively, in our simulations. As described in Section 2.1, we have adopted the log-normal mass function of Covey et al. (2008), and they cite a range of possible values for the best fit mass function parameters: $0.08\text{--}0.12 \log(M/M_\odot)^{-1} \text{ pc}^{-3}$ for the normalization (A), $0.20\text{--}0.50 M_\odot$ for the peak (M_c), and $0.22\text{--}0.37$ for the width ($\sigma_{\log M}$). If we vary the parameters within these limits the number of objects within 100 pc varies from 2.7×10^5 to 5.0×10^5 (i.e., about $\pm 30\%$). Thus, the yields from our simulations are correspondingly uncertain by $\pm 30\%$ from the normalization of the mass function alone.

We also tried the power-law mass function derived by Reid et al. (1999), which predicts 4.1×10^5 low-mass stars and brown dwarfs ($0.01 < M/M_\odot < 1.0$) within 100 pc. This is very similar to the total number derived from the log-normal mass function because, as Covey et al. (2008) pointed out, the data used to derive both functions are in good agreement even though the analytic expressions adopted by the authors differ. These different analytic expressions result in objects being apportioned differently over the mass range we consider ($0.01 < M < 1.0 M_\odot$). The essentially flat (in $\log M$) power-law mass function of Reid et al. (1999) results in roughly an equal number of objects in the range $0.01\text{--}0.1 M_\odot$ as in the range $0.1\text{--}1.0 M_\odot$, whereas the log-normal mass function, which peaks at $0.29 M_\odot$, results in more than $10\times$ the number of objects in the upper range compared to the lower range. Thus, the choice of mass function can change the number of low-mass stars by a factor of ~ 2 and the number of brown dwarfs by a factor of ~ 10 .¹² Correspondingly, we found that the eclipsing binary yield was reduced by about 50% (as expected), while the reduction in the transit yield was smaller (about 30%) because the increase in later type M dwarfs somewhat compensated for the reduction in mid-M dwarfs. In addition, the factor of ~ 10 increase in the numbers of brown dwarfs resulted in ~ 3 predicted detections of substellar eclipsing binaries not seen when using the log-normal mass function.

- *Binary parameters.* The eclipsing binary yield also depends on the binary properties we have adopted for M dwarfs, which is ultimately based on the period distribution of Duquennoy & Mayor (1991, DM91) and the mass ratio distribution of Fischer & Marcy (1992, FM92). The FM92 mass ratio distribution has not been corrected for observation bias or completeness and is dominated by wide, long-period systems. A recent compilation of known low-mass eclipsing binaries (López-Morales 2007) shows the clear preference of such systems toward

¹²In fact, we chose to adopt the log-normal mass function because it is the most consistent with the best available data for M dwarfs (Covey et al. 2008), and it is also consistent with the number density of T dwarfs in the solar neighborhood (Metchev et al. 2008; Pinfield et al. 2008), whereas a power-law mass function flat in $\log M$ predicts significantly more T dwarfs than are observed.

mass ratios of unity, and in fact, this phenomenon of short-period “twins” is expected from binary formation theory (Artymowicz 1983; Bate 2000). Having more twins would mean that more M dwarf eclipsing binaries would be easier to detect (as the larger companion radii would lead to deeper eclipses), but that there should be fewer (if any) brown dwarfs found in eclipsing systems with M dwarfs.

The assumed binary period distribution can also affect the predicted yield significantly, since the number of eclipsing binaries strongly depends on its short-period tail. Therefore, we also tried adopting a compressed DM91 distribution for M dwarfs, similar to the approach of Basri & Reiners (2006) for very low-mass stars, who based their distribution on the models of Fisher (2004) that predict shorter period orbits for lower mass binaries. Using a DM91 period distribution shifted and compressed by 0.5 in $\log P$ (i.e., assuming typical masses for the FM92 and DM91 samples of $\sim 0.3 M_{\odot}$ and $\sim 1.0 M_{\odot}$), we found essentially the same eclipsing binary yield. Although the tails of the distribution were reduced, the shift to shorter periods roughly compensated, yielding the same number of short-period M dwarf binaries.

- *Substellar binaries.* Although our simulations do not predict any eclipsing binaries composed solely of brown dwarfs, the scarcity of data for brown dwarf spectroscopic binaries renders the orbital period distribution, particularly at short periods, very uncertain. In fact, combined with the uncertainty in the substellar portion of the mass function, some brown dwarf eclipsing binaries may indeed be detected by the PS1 3π Survey. Because of the flat mass–radius relation for brown dwarfs, substellar eclipsing binaries should be among the easiest eclipsing systems to detect: equal radii imply eclipse depths of 50–100% (depending on the flux ratio) over a wide range of mass ratios.
- *Survey cadence.* Our assumption of uniform phase coverage may impact the survey detection sensitivity. In particular, for each bandpass the PS1 3π Survey as planned will obtain images in pairs separated by 30–60 minutes for the purpose of asteroid detection. In our simulations, we have treated these two epochs as independent because this interval is comparable to or larger than the expected eclipse durations. For systems detected in our simulations, median eclipse durations were 45 minutes for transiting planets and 30 minutes for eclipsing binaries. Thus, it is unlikely (but not impossible) that an eclipse event could be detected in both images of a 3π Survey observation pair, which would enable more robust detections of candidate eclipsing systems. We have conservatively chosen not to model this effect, although it may play an important role in both eclipse detection and false positive rejection in actual survey data.
- *Seeing/saturation.* We have assumed typical seeing of $0''.8$ for PS1, located on Haleakala, on the island of Maui (Appendix A). Current on-sky assessments of the image quality indicates a more realistic estimate may be $1''.0$. The seeing has a significant impact on the saturation limits, and such a change would make these less restrictive by 0.4 mag.¹³ This would make

¹³Seeing of $1''.0$ also changes the $S/N = 5$ detection limits, by 0.2 mag, but this does not significantly impact our

more of the earlier type and/or nearer M dwarfs accessible to the 3π Survey, increasing the number of detectable transiting planets and eclipsing binaries. For example, Table 1 shows that 22% of M dwarfs within 100 pc are saturated assuming $0''.8$ seeing, and this would change to 15% for $1''.0$ seeing. Thus, more M dwarfs would be unsaturated in more bandpasses.

4.2. Follow-up Observations

Eclipse events are only expected to be observed once, or possibly twice, per star over the entire course of the PS1 3π survey. This has two consequences: (1) the eclipse signatures of transiting planets and eclipsing binaries will be indistinguishable from each other in PS1 data; and (2) detailed photometric and spectroscopic follow-up observations will be required to characterize all systems. Since eclipsing binaries are predicted to outnumber transiting planets by $\sim 20:1$ in survey data, the initial step of distinguishing between these two classes of objects, which have very different RV precision requirements, should be done as efficiently as possible. Since all of the objects we have considered will have parallaxes measured by PS1, it may be possible to distinguish eclipsing binaries from transit hosts since they will appear overluminous on the color–magnitude diagram, especially if the binaries are preferentially twins (as discussed in Section 4.1). However, we conservatively assume that robust discrimination will only be possible with photometric and/or spectroscopic follow-up observations.

Transiting planets may be distinguished from binaries either by their much lower RV semi-amplitude (via spectroscopic follow-up) or by the shape of the light curve and lack of a secondary eclipse (via photometric follow-up). With unknown ephemerides, RV measurements from at least two, possibly three, epochs would be needed to identify eclipsing binaries. Assuming 20 pairs of RV measurements could be obtained per night, at least 14 nights would be required to follow-up all 273 candidates. This would be a substantial investment of resources, even if the brightest targets could be done with smaller aperture telescopes (e.g., CFHT/Espadons) instead of large apertures (e.g., Keck/HIRES). In fact, this RV follow-up would be much more powerful if it were obtained *after* ephemerides were determined from photometric follow-up. The RV observation epochs could then be optimally timed to sample maxima in the RV curves, and these two RV measurements along with a light curve would yield a full orbital solution (assuming circular orbits).

Photometric follow-up would be most efficiently broken into two campaigns: first, to determine rough ephemerides (transit times and periods); second, to measure higher precision and cadence light curves during transit. The initial campaign would require regular monitoring every eclipse half-interval (15 minutes) over at most two full periods (0.4 days for binaries; 3 days for planets), in order to catch two eclipses. Assuming 5 minutes per observation (slewing and integration time), this amounts to 6.4 hours per binary and 48 hours per planet, for a total of 230 nights. With

results as M dwarfs within 100 pc are well above the detection threshold.

ephemerides in hand, detailed light curves can then be obtained. In order to measure both the primary and secondary eclipses of binaries, at least two such light curves are required, so this second phase would cost ≈ 2 hours per object, for a total of 55 nights. Thus, all the necessary photometric follow-up could cost as much as 285 nights, essentially all the clear nights in a year for a single telescope. However, particularly for the initial campaign of 230 nights, this cost could be distributed among several small telescopes, possibly even in collaboration with amateur astronomers – a strategy employed with success by the XO transit survey (McCullough et al. 2006) and the MicroFUN¹⁴ consortium. This is possible because eclipsing systems discovered in the 3π Survey would be relatively bright: PS1 achieves a S/N $\gtrsim 100$ in 30 s with a 1.8-m telescope, so ≈ 30 cm apertures should be able to achieve a photometric precision of $\approx 2\%$ in just a few minutes.

To summarize the initial follow-up requirements, either an RV campaign costing at least 14 nights on 8-m class telescopes or a photometric campaign costing $285/N$ nights on N small-aperture ($\gtrsim 30$ cm) telescopes is needed to separate all the transiting planets from the 20:1 more numerous eclipsing binaries. We suggest that the photometric monitoring campaign be conducted first, so that eclipsing binaries can be identified by the presence of a shallower secondary eclipse, and also so that ephemerides can be determined for both the transiting planets and eclipsing binaries. A subsequent RV monitoring campaign can then focus only on the planets and a subset of the most interesting eclipsing binaries, thus reducing the amount of large-aperture telescope time needed.

For the eclipsing binaries that are predicted to be discovered by the PS1 3π Survey, the RV precision necessary for precise parameter determination is attainable with current instrumentation. Our simulations predicted a median binary orbital period of 0.4 days, semimajor axis of 0.006 AU, primary mass of $0.2 M_{\odot}$, mass ratio of 0.7, and inclination of 86° , resulting in a typical RV semi-amplitude (K_1) of 80 km s^{-1} . This is very similar to the eclipsing binary for which Becker et al. (2008) recently achieved $\sim 3 \text{ km s}^{-1}$ precision using Keck/HIRES, even though their target ($r = 18.3$ mag) is ≈ 2.5 mag fainter than those predicted to be found by PS1 (median $r = 15.8$ mag; Figure 7).

For transiting Jupiters the RV precision requirements are much more demanding. Our simulations predicted a median planet orbital period of 3 days, semimajor axis of 0.02 AU, host star mass of $0.2 M_{\odot}$ (and thus a mass ratio of 0.005), and inclination of 89° , resulting in a typical RV semi-amplitude of 0.4 km s^{-1} . While current planet searches have used optical spectroscopy to achieve a precision of 5–10 m s^{-1} for M dwarfs (e.g., Butler et al. 2004; Bonfils et al. 2005), such targets are $\gtrsim 100\times$ brighter than the M dwarf host stars from our simulations. For an M dwarf of comparable brightness to such PS1 candidates, Blake et al. (2008a) have recently demonstrated a precision of 0.3 km s^{-1} using high-resolution near-infrared spectroscopy. While this is the current state of the art, much better precision will be needed to measure the RV signal of transiting Jupiters around M dwarfs. Future near-infrared spectrographs aim to reach a precision of 1 m s^{-1} (i.e., comparable to that of current optical spectrographs), which would enable the detection of

¹⁴<http://www.astronomy.ohio-state.edu/~microfun/>

planets around M dwarfs down to an Earth mass (e.g., Jones et al. 2008).

4.3. Extending the Volume-limited Sample

In the case of the PS1 3π Survey, we have only considered a volume-limited sample extending to 100 pc, the distance within which parallaxes will be reliably measured. However, M dwarfs remain detectable at even greater distances (see Figure 10), so one could considerably expand the search volume and in turn the number of eclipse/transit detections. Although objects in such an expanded sample will be more difficult to follow-up due to their faintness, it may be the only way to discover especially rare objects such as substellar eclipsing binaries.

Optical and/or near-infrared colors can reliably discriminate between nearby M type dwarfs and background giants (e.g., Bessell & Brett 1988; Cruz et al. 2003). Thus, combining the PS1 optical bandpasses with photometry from 2MASS may enable a robust color-selected sample of M dwarfs out to the detection limit of the shallower survey, which in this case is 2MASS (Figure 10). The 2MASS point source catalog is complete for mid-M dwarfs to a distance of ≈ 200 pc (130 pc for M6, 280 pc for M4). Expanding the volume-limited sample to this distance would increase the survey volume by a factor of ≈ 8 .

The PS1 3π Survey will of course measure proper motions for many more stars than it will measure parallaxes. Assuming an astrometric precision of 10 mas per epoch and an operational lifetime of 3 years, PS1 will be able to measure proper motions of $\gtrsim 0''.03 \text{ yr}^{-1}$ ($S/N > 10$). M dwarfs in the volume-limited sample of Reid et al. (1995) have a median tangential velocity of about 40 km s^{-1} , which translates to $0''.03 \text{ yr}^{-1}$ at a distance of 300 pc. The PS1 3π Survey photometric detection limits for mid-M dwarfs are well beyond 300 pc (e.g., M6 stars can be detected to 770 pc). Thus, a proper motion selected sample would contain most of the M dwarfs within 300 pc, which is about $\gtrsim 20\times$ more M dwarfs than in the parallax selected sample. However, eclipsing systems discovered in such an extended sample will be $\sim 10\times$ fainter than objects discovered within 100 pc, which will make spectroscopic follow-up more challenging.

5. Conclusions

We have developed detailed simulations to predict the yield of eclipsing systems in sparsely sampled multi-epoch all-sky surveys, and we have applied these to the Pan-STARRS-1 (PS1) 3π Survey. We created a model of the solar neighborhood that includes low-mass stars, brown dwarfs, and a realistic population of binary companions. We devised a method to compute the number of transiting planets in this sample semi-analytically, in addition to simulating actual survey light curves using Monte Carlo methods. In Appendix B, we have investigated various algorithms for searching sparsely sampled light curves for eclipse events and carefully considered the vulnerability of these techniques to the most likely source of astrophysical false positives, star spots.

Because upcoming multi-epoch surveys such as PS1 will achieve an astrometric precision of 10 mas per epoch, they will measure parallaxes for the hundreds of thousands of stars within 100 pc. Such an unprecedented sample of nearby stars will provide the means for an innovative approach to eclipse hunting by focusing only on the closest, best characterized stars. In our simulations, we have only considered this 100-pc sample, although it may be possible to expand the search volume – and thus the predicted survey yields – by an order of magnitude or more by using color selection and/or the proper motions also measured by these surveys. Restricting an eclipse search to a volume-limited sample naturally reduces the exotic astrophysical false positives that have afflicted previous transit surveys. However, the gain in areal coverage comes at the price of sparse light curve sampling, resulting in single-epoch eclipse detections. Thus, a low rate of photometric outliers in survey data is essential, and extensive follow-up observations will be needed to characterize candidate eclipsing systems.

A volume-limited sample is dominated by the most abundant stars: M dwarfs. Assuming an intrinsic frequency of 0.47% for Jupiter-like planets in short-period orbits ($P < 11.5$ days) around M dwarfs, our simulations predict that about 13 transiting planets would be detectable in the PS1 3π Survey. Under the same assumptions, an RV survey would need to monitor $\sim 30,000$ M dwarfs to discover an equivalent number of transiting Jupiters around M dwarfs. Although the host stars of the transiting Jupiters discovered by PS1 would be $\sim 100\times$ fainter than the M dwarf hosts of known extrasolar planets, they would be sufficiently bright to permit spectroscopic follow-up with currently available near-infrared spectrographs. The properties of planets around M dwarfs are poorly constrained by current observations, and the expected planet yield is correspondingly uncertain. For example, if we assume a simple linear scaling with host star mass of the inner edge of protoplanetary disks, which is thought to define the terminus of planet migration, the orbital periods of close-in M dwarf planets would be $\sim 3\times$ shorter than their solar-type counterparts, resulting in a factor of ~ 4 increase in the transit yield from our simulations.

Our simulations also predict that hundreds of low-mass eclipsing binaries with individual masses $< 0.5 M_{\odot}$ are potentially detectable in the PS1 3π Survey 100-pc sample. This would be a major step forward in testing models of low-mass stars, which currently rely on mass and radius measurements from only seven such systems. In fact, only a few of these systems have parameters determined to high precision because of their apparent faintness, whereas eclipsing binaries discovered in a volume-limited sample by PS1 would naturally include some of the brightest eclipsing binaries in the sky. The number of detectable substellar eclipsing binaries is uncertain (ranging from none to ~ 3 for the 3π Survey) due to poor observational constraints on substellar regime of the initial mass function and on the properties of brown dwarf binaries at such small orbital separations. The mass ratio distribution for tight M dwarf binaries is nearly as uncertain, but using the best available data our simulations predict that dozens of brown dwarfs are potentially detectable in eclipsing binaries with M dwarfs. Such systems would enable radius measurements of field brown dwarfs for the first time, providing sorely needed tests of substellar evolutionary models.

This is the first detailed analysis of the expected yield of eclipsing systems from Pan-STARRS, revealing its potential to discover systems that have largely eluded previous surveys. The extensive set of tools we have developed for our simulations can be readily applied to other sparsely sampled, multi-epoch all-sky surveys planned for the coming decade. Surveys such as LSST are anticipated to far exceed the revolutionary surveys of the present by imaging the whole sky deeper and more often, opening the door to intrinsically fainter and rarer eclipsing systems.

We have benefited from conversations with Eugene Magnier about the PS1 surveys, J. Patrick Henry and Thierry Forveille about statistics, Eric Hilton about M dwarf variability and flares, and Adam Kraus about low-mass binaries. We are grateful to John Tonry for providing information about the PS1 photometric system. Our research has employed NASA’s Astrophysical Data System; the SIMBAD database operated at CDS, Strasbourg, France; the SpeX Prism Spectral Libraries, maintained by Adam Burgasser at <http://www.browndwarfs.org/spexprism>; Sandy Leggett’s L and T dwarf archive at <http://www.jach.hawaii.edu/skl/LTdata.html>; and the M, L, and T dwarf compendium housed at DwarfArchives.org and maintained by Chris Gelino, Davy Kirkpatrick, and Adam Burgasser (Kirkpatrick 2003; Gelino et al. 2004). TJD and MCL acknowledge support for this work from NSF grant AST-0507833, and MCL acknowledges support from an Alfred P. Sloan Research Fellowship.

A. The Pan-STARRS-1 3π and Medium Deep Surveys

In the following, we describe the attributes of the PS1 photometric system and the 3π and Medium Deep surveys. PS1 is a 1.8-m telescope located on Haleakala on the island of Maui, and has an effective collecting area of 1.73 m^{-2} , after accounting for obscuration and diffraction losses. It is equipped with the Gigapixel Camera #1 (GPC1), comprising 60 orthogonal transfer array (OTA) chips, each $4\text{k}\times 4\text{k}$ pixels, sampling a circular field-of-view 3° in diameter. GPC1 has a nominal pixel scale of $0''.26 \text{ pixel}^{-1}$, read noise (σ_r) of $5 \text{ e}^- \text{ pixel}^{-1}$, and gain of $1 \text{ e}^- \text{ DN}^{-1}$ (Onaka et al. 2008). We have assumed that the best possible photometric precision for PS1 is 0.01 mag, i.e., a systematic noise floor of $(\text{S/N})_{\text{floor}} = 100$ in the photometry.

The PS1 photometric system is largely patterned after the SDSS photometric system (Fukugita et al. 1996), but the PS1 detectors are much more red-sensitive so low-mass stars and brown dwarfs will have somewhat different colors in the PS1 photometric system than in SDSS. The total predicted system throughput in each of the five PS1 bandpasses (*grizy*) is shown in Figure 8 along with the SDSS bandpasses. Compared to SDSS, PS1 has significantly increased sensitivity at *z*-band, along with an additional bandpass (*y*) centered at $0.98 \mu\text{m}$. We have computed the AB system zero points of these bandpasses, as well as the expected sky flux in each filter. These quantities are listed in Table 5.

For our simulations, we drew on the extensive body of optical photometry from SDSS for low-mass stars and brown dwarfs (Hawley et al. 2002; Knapp et al. 2004; Chiu et al. 2006). Therefore, we have derived conversions from the SDSS to the PS1 photometric systems as a function of spectral type by computing synthetic photometry from publicly available spectra. We used the averaged stellar spectra of G0–M6 dwarfs from Pickles (1998), which has essentially complete wavelength coverage at optical and near-infrared wavelengths. We used optical spectra retrieved from dwarfarchives.org for K5–M9 dwarfs, most of which are either unpublished or are from Kirkpatrick et al. (1991), Henry et al. (1994), or Kirkpatrick et al. (1995). We used flux-calibrated spectra of M, L, and T dwarfs both from S. K. Leggett’s spectral library,¹⁵ which comprise a variety of published spectra, and from the IRTF/Spex spectral library (Cushing et al. 2005, J. T. Rayner et al. 2009, submitted).¹⁶

Our derived SDSS-to-PS1 photometric conversions are shown in Figure 9, along with polynomial fits as a function of spectral type (coefficients given in Table 6). These conversions reflect how the flux ratio between an object of a given spectral type and a zero-magnitude source differs from SDSS to PS1. By definition, the AB zero-magnitude source is blue ($F_\lambda \propto \lambda^{-2}$), while M, L, and T dwarfs are red at optical wavelengths. Thus, PS1 filters that are somewhat redder than their SDSS counterparts (like *g* and *r*) gain object flux without as much change in the zero-magnitude flux, leading to brighter PS1 magnitudes of up to 0.3 mag for the reddest objects. The PS1 *i* band

¹⁵<http://www.jach.hawaii.edu/~sk1/LTdata.html>

¹⁶http://irtfweb.ifa.hawaii.edu/~spex/IRTF_Spectral_Library/

is very similar to SDSS, resulting in $\lesssim 0.1$ mag differences in zero point.¹⁷ The biggest photometric conversion factor is for the z band, which is understandable since for SDSS this is a longpass filter but for PS1 it has well defined cut-on and cut-off wavelengths.

The Pan-STARRS-1 Telescope will be used to conduct several surveys, and the largest two of these are the 3π Survey and the Medium Deep Survey, nominally using 56% and 25% of the available observing time, respectively. At the time of writing, the exact survey strategies to be employed are somewhat uncertain, pending on-sky tests of PS1 performance. For our simulations, we have assumed the surveys will be conducted as conceived in the Design Reference Mission document. The cadence employed by the 3π Survey is planned to be optimized for parallax measurements of nearby low-mass objects, with redder bands sampling epochs nearer the maximum parallax factor. Thus, observations in each of the five bandpasses will be spread out over each observing season. Also, each observation is expected to consist of a pair of images taken in the same bandpass within 30–60 minutes of each other, in order to identify asteroids, and we count these as separate epochs. The expected Medium Deep Survey cadence is to simply rotate through the five filters every four days.

Tables 7 and 8 summarize the relevant information for each survey, as well as detection and saturation limits that we derived. For the detection limits, we have assumed an aperture that is 1 FWHM in diameter, which for a 2-dimensional Gaussian collects 50% of the source flux. We also tabulate the earliest spectral type that is unsaturated at 100 pc, which is the limiting distance at which PS1 is able to measure $S/N = 10$ parallaxes. Unless the seeing is worse than the nominal $0''.8$ (see Section 4.1), objects earlier than this will not have measurable parallaxes because they will be saturated. Loss of time due to weather has been accounted for in the survey parameters.

Using the survey information given in Tables 7 and 8 and the empirical relations in Section 2.1, we have derived detection limits as a function of spectral type for each PS1 bandpass. Figure 10 shows the distances at which objects of a given spectral type are expected to reach the detection threshold ($S/N = 5$), as well as the distances within which they are so bright that they will be saturated. Because the color selection of nearby stars may benefit from, or require, the use of near-infrared photometry, we also show the distance limit at which 2MASS is 99% complete in J band ($J < 15.8$ mag). We chose not to show the K -band limit for simplicity, although it is very similar to the J -band limit (except for T dwarfs) due to the trade off between a brighter sky background but more object flux for red objects at K band.

¹⁷We note that a simple polynomial fit to the i band synthetic photometry does not accurately reproduce details in the i band photometric conversion as a function of spectral type. However, the discrepancies between our fit and the actual photometry are $\lesssim 0.06$ mag, and thus have an insignificant impact on our results.

B. Algorithms for Detecting Eclipses in Sparsely Sampled Light Curves

We have investigated algorithms for detecting eclipse signatures in sparsely sampled light curves, such as those generated by upcoming multi-epoch all-sky surveys. This problem is inherently different from searching for a low-amplitude periodic signal in a densely sampled light curve, for which robust methods have been developed for current planetary transit surveys (e.g, Kovács et al. 2002). Rather, a sparsely sampled light curve will likely only catch one eclipse event at a single epoch, so we are interested in identifying a single discrepant point for an otherwise constant star. Below we describe three algorithms for identifying such eclipses and then assess their detection limits and vulnerability to false positives.

1. χ^2 *null test*. The χ^2 of a light curve may be reliably computed when measurement errors are well determined:

$$\chi^2 = \sum_{i=1}^n \frac{(N_i - \bar{N})^2}{\sigma_i^2} \quad (\text{B1})$$

where N_i and σ_i are the counts (DN) and uncertainty at each light curve point, and \bar{N} is the weighted average of the light curve. Any deviation from a constant light curve will increase the value of χ^2 . For example, an increase in χ^2 could signify a single very discrepant point (e.g., a deep eclipse) or variability throughout the light curve. The value of χ^2 gives the confidence interval for the null hypothesis that the flux from the star is constant.

2. S^2 *index*. Bramich et al. (2005) introduced an eclipse detection statistic (S^2) which combines the χ^2 values of different portions of the light curve to give an index which is roughly equivalent to the $(S/N)^2$ of the detection. We adopt the form of the S^2 index as modified by Bramich et al. (2008), which was used to assess the presence of eclipses and flares in sparsely sampled light curves in SDSS Stripe 82:

$$S^2 = \frac{\chi_{\text{const}}^2 - \chi_{\text{out}}^2}{\chi_{\text{out}}^2 / \nu_{\text{const}}} \quad (\text{B2})$$

where χ_{const}^2 is the same as Equation B1, χ_{out}^2 is computed excluding the minimum point in the light curve, and ν_{const} is the number of degrees of freedom of χ_{const}^2 (i.e., $n - 1$ for a light curve with n points). The S^2 index is designed to be more robust against false positives due to variability than the χ^2 null tests, since S^2 is only large when the out-of-transit portion of the light curve is nearly constant (small χ_{out}^2). To determine whether an eclipse was detected, a threshold value of S^2 must be chosen (e.g., a S^2 value of 100 corresponds to a S/N of ~ 10).

3. S/N *model*. The S/N of a candidate eclipse event can be computed directly from the light curve and its errors:

$$\frac{S}{N} = \frac{\bar{N}_{\text{out}} - N_{\text{min}}}{\sqrt{\sigma_{\text{out}}^2 + \sigma_{\text{min}}^2}} \quad (\text{B3})$$

where N_{\min} and σ_{\min} are the counts (DN) and error at light curve’s minimum point, $\overline{N}_{\text{out}}$ is the mean of the remaining points, and σ_{out} is the standard error of the mean. In our S/N model, σ_{out} and σ_{\min} are limited by the systematic noise floor ($S/N_{\text{floor}} = 100$ for PS1). For example, the uncertainty in the out-of-transit counts (σ_{out}) is not allowed to be smaller than $\overline{N}_{\text{out}}/(S/N_{\text{floor}})$. The eclipse S/N computed using this model will be small for a constant light curve and large when the minimum point is very different from the remaining points. A threshold S/N must be chosen to determine whether an eclipse was detected.

The ideal eclipse detection algorithm is sensitive to the smallest flux diminutions, while also being robust against false positives. In Figure 11, we show the minimum detectable eclipse depths of the various algorithms for a source with a photometric S/N of 100 (i.e., at the photometric error floor of PS1). As points are added to the light curve, the sensitivity of the algorithms change in different ways. For the S^2 index, the sensitivity monotonically improves, while for the χ^2 null test the sensitivity actually gets worse. This is simply due to the fact that by adding more constant flux points to the light curve, the significance of the single discrepant point is decreased compared to the null hypothesis of constant flux. The S/N model gives essentially the same sensitivity for any light curve because in this case we have considered a source whose photometric errors are already at the noise floor; thus, adding more points does not reduce the noise. In Figure 11, we have chosen a S^2 threshold of 150 in order to roughly match the sensitivity of the S/N model threshold of 10 and χ^2 null test confidence limit of 10σ . Of course, the exact choice of the detection threshold should be based on the expected number of false positives.

In practice, the number of false positives resulting from different detection algorithms depends on the particular survey strategy and the nature of the contaminating sources. In our simulations, we have found that PS1 will be particularly sensitive to transiting Jupiters around M dwarfs. A large fraction of M dwarfs are chromospherically active (e.g., Gizis et al. 2000), thus they are expected to show photometric variability due to spots, making this one of the most likely sources of false positive eclipse detections in sparsely sampled data. In Figure 12, we show contours of the false positive fraction due to spots for the 3π Survey’s 12-point light curves. The variability due to spots is assumed to be sinusoidal, and we have considered a range of amplitudes, properly accounting for the fact that a sine curve has an rms of $\sin(\frac{\pi}{4})$. We adopt the best available estimate of variability among M dwarfs from Rockenfelder et al. (2006) who found a median variability amplitude of 0.014 mag (0.005–0.02 mag observed range) for $21\pm 11\%$ of M dwarfs. The contours in Figure 12 show the fraction of false positives over a range of parameter space that covers low to high amplitude variability and rare to common occurrence fractions of variability.

For the 3π Survey, Figure 12 shows that the χ^2 null test is vulnerable to false positives over a broader range of variability parameter space than the other algorithms. This is intuitively expected as it is sensitive to any deviations from a constant light curve, not just eclipses. The S^2 index and S/N model yield false positives over about the same amount of parameter space, but in different regions. The S/N model is vulnerable to very rare, highly variable objects. For example, if 1 in 10^3 M dwarfs are variable at the 0.10 mag level, this would result in an unmanageable false

positive fraction of $\sim 10^{-3}$. Such a population could easily have been missed by the best available variability surveys, which have targeted only a few dozen M dwarfs. On the other hand, the S^2 index is vulnerable to relatively common objects with a lower level of variability. We also experimented with arbitrarily increasing the number of light curve points and found the most drastic improvement for the S^2 index which for light curves with > 15 points had a false positive rate $< 10^{-6}$ over the entire variability parameter space in Figure 12. The improvement for the S/N model was less extreme, with contours changing by only 0.02 mag for 72-point light curves, and the χ^2 null test actually worsened.

In summary, we have investigated three algorithms for eclipse detection in sparsely sampled light curves with very few (~ 10) epochs. We have paid particular attention to possible contamination from variability due to star spots, which is the most likely source of eclipse false positives in such data for M dwarfs. All algorithms achieve similar eclipse depth sensitivities for a given confidence interval (Figure 11). We found that the χ^2 null test is a good general tool for identifying deviations from a constant light curve, but because of this it has the highest false positive rate. The S^2 index and S/N model are vulnerable to different source populations of false positives (e.g., rare, highly variable objects), which are largely unprobed by current variability surveys. Thus, it is impossible to predict the better algorithm for robustly detecting transits in advance of actual survey data. In fact, using *both* algorithms simultaneously may prove to be the best strategy for eliminating false positives. We emphasize that the proper eclipse detection algorithm depends not only on the underlying source of false positives, but also on the particular survey strategy. For example, in the PS1 3π Survey observation epochs will actually be obtained in pairs separated by 30–60 minutes for the purpose of asteroid detection. This may help distinguish spots from true eclipse events since stellar rotation for M dwarfs occurs over much longer time scales ($P \gtrsim 1$ day, e.g., Delfosse et al. 1998b), and thus spots would cause a flux dip in both images in the pair, whereas a transit would only be detected in one (e.g., see the discussion on paired observations by Welch & Stetson 1993).

REFERENCES

- Allen, P. R. 2007, *ApJ*, 668, 492
- Andersen, J. 1991, *A&A Rev.*, 3, 91
- Andrews, S. M., & Williams, J. P. 2005, *ApJ*, 631, 1134
- Artymowicz, P. 1983, *Acta Astronomica*, 33, 223
- Bailey, J., Butler, R. P., Tinney, C. G., Jones, H. R. A., O’Toole, S., Carter, B. D., & Marcy, G. W. 2009, *ApJ*, 690, 743
- Baraffe, I., Chabrier, G., Allard, F., & Hauschildt, P. H. 1998, *A&A*, 337, 403
- Baraffe, I., Chabrier, G., Barman, T. S., Allard, F., & Hauschildt, P. H. 2003, *A&A*, 402, 701
- Basri, G., & Reiners, A. 2006, *AJ*, 132, 663
- Bate, M. R. 2000, *MNRAS*, 314, 33
- Beatty, T. G., & Gaudi, B. S. 2008, *ApJ*, 686, 1302
- Becker, A. C., et al. 2008, *MNRAS*, 386, 416
- Bessell, M. S. 1991, *AJ*, 101, 662
- Bessell, M. S., & Brett, J. M. 1988, *PASP*, 100, 1134
- Blake, C. H., Charbonneau, D., White, R. J., Torres, G., Marley, M. S., & Saumon, D. 2008a, *ApJ*, 678, L125
- Blake, C. H., Torres, G., Bloom, J. S., & Gaudi, B. S. 2008b, *ApJ*, 684, 635
- Bochanski, J. J., West, A. A., Hawley, S. L., & Covey, K. R. 2007, *AJ*, 133, 531
- Bonfils, X., et al. 2005, *A&A*, 443, L15
- Bouchy, F., Pont, F., Melo, C., Santos, N. C., Mayor, M., Queloz, D., & Udry, S. 2005, *A&A*, 431, 1105
- Bramich, D. M., et al. 2005, *MNRAS*, 359, 1096
- . 2008, *MNRAS*, 386, 887
- Burgasser, A. J., Reid, I. N., Siegler, N., Close, L., Allen, P., Lowrance, P., & Gizis, J. 2007, in *Protostars and Planets V*, ed. B. Reipurth, D. Jewitt, & K. Keil, 427–441
- Burke, C. J. 2008, *ApJ*, 679, 1566

- Butler, R. P., Vogt, S. S., Marcy, G. W., Fischer, D. A., Wright, J. T., Henry, G. W., Laughlin, G., & Lissauer, J. J. 2004, *ApJ*, 617, 580
- Butler, R. P., et al. 2006, *ApJ*, 646, 505
- Chabrier, G., Baraffe, I., Allard, F., & Hauschildt, P. 2000, *ApJ*, 542, 464
- Charbonneau, D., Brown, T. M., Burrows, A., & Laughlin, G. 2007, in *Protostars and Planets V*, ed. B. Reipurth, D. Jewitt, & K. Keil, 701–716
- Charbonneau, D., Brown, T. M., Latham, D. W., & Mayor, M. 2000, *ApJ*, 529, L45
- Chiu, K., et al. 2006, *AJ*, 131, 2722
- Claret, A. 2004, *A&A*, 428, 1001
- Close, L. M., Siegler, N., Freed, M., & Biller, B. 2003, *ApJ*, 587, 407
- Covey, K. R., et al. 2008, *AJ*, 136, 1778
- Cox, A. N. 2000, *Allen’s Astrophysical Quantities* (4th ed.) (New York: Springer)
- Creevey, O. L., et al. 2005, *ApJ*, 625, L127
- Cruz, K. L., Reid, I. N., Liebert, J., Kirkpatrick, J. D., & Lowrance, P. J. 2003, *AJ*, 126, 2421
- Cumming, A., Butler, R. P., Marcy, G. W., Vogt, S. S., Wright, J. T., & Fischer, D. A. 2008, *PASP*, 120, 531
- Cushing, M. C., Rayner, J. T., & Vacca, W. D. 2005, *ApJ*, 623, 1115
- de Jager, C., & Nieuwenhuijzen, H. 1987, *A&A*, 177, 217
- Delfosse, X., Forveille, T., Mayor, M., Burnet, M., & Perrier, C. 1999, *A&A*, 341, L63
- Delfosse, X., Forveille, T., Mayor, M., Perrier, C., Naef, D., & Queloz, D. 1998a, *A&A*, 338, L67
- Delfosse, X., Forveille, T., Perrier, C., & Mayor, M. 1998b, *A&A*, 331, 581
- Dong, S., et al. 2009, *ApJ*, 695, 970
- Dupuy, T. J., Liu, M. C., & Ireland, M. J. 2009a, *ApJ*, 692, 729
- . 2009b, *ApJ*, 699, 168
- Duquennoy, A., & Mayor, M. 1991, *A&A*, 248, 485
- Faherty, J. K., Burgasser, A. J., Cruz, K. L., Shara, M. M., Walter, F. M., & Gelino, C. R. 2009, *AJ*, 137, 1

- Fischer, D. A., & Marcy, G. W. 1992, *ApJ*, 396, 178
- Fisher, R. T. 2004, *ApJ*, 600, 769
- Ford, H. C., Bhatti, W., Hebb, L., Petro, L., Richmond, M., & Rogers, J. 2008, in *American Institute of Physics Conference Series*, Vol. 1082, American Institute of Physics Conference Series, 275–281
- Fukugita, M., Ichikawa, T., Gunn, J. E., Doi, M., Shimasaku, K., & Schneider, D. P. 1996, *AJ*, 111, 1748
- Gaudi, S. 2007, in *Astronomical Society of the Pacific Conference Series*, Vol. 366, *Transiting Extrapolar Planets Workshop*, ed. C. Afonso, D. Wel Drake, & T. Henning, 273
- Gelino, C. R., Kirkpatrick, J. D., & Burgasser, A. J. 2004, *BAAS*, 205
- Gillon, M., et al. 2007, *A&A*, 472, L13
- Gimenez, A., & Garcia-Pelayo, J. M. 1983, *Ap&SS*, 92, 203
- Gizis, J. E., Monet, D. G., Reid, I. N., Kirkpatrick, J. D., Liebert, J., & Williams, R. J. 2000, *AJ*, 120, 1085
- Gizis, J. E., Reid, I. N., & Hawley, S. L. 2002, *AJ*, 123, 3356
- Golimowski, D. A., et al. 2004, *AJ*, 127, 3516
- Guenther, E. W., & Wuchterl, G. 2003, *A&A*, 401, 677
- Hawley, S. L., et al. 2002, *AJ*, 123, 3409
- Hayes, D. S. 1985, in *IAU Symposium*, Vol. 111, *Calibration of Fundamental Stellar Quantities*, ed. D. S. Hayes, L. E. Pasinetti, & A. G. D. Philip, 225–249
- Hebb, L., Wyse, R. F. G., Gilmore, G., & Holtzman, J. 2006, *AJ*, 131, 555
- Henry, T. J., Kirkpatrick, J. D., & Simons, D. A. 1994, *AJ*, 108, 1437
- Ida, S., & Lin, D. N. C. 2005, *ApJ*, 626, 1045
- Irwin, J., et al. 2009a, *ApJ*, 701, 1436
- Irwin, J., Charbonneau, D., Nutzman, P., & Falco, E. 2009b, in *IAU Symposium*, Vol. 253, *IAU Symposium*, 37–43
- Joergens, V. 2006, *A&A*, 448, 655
- Johnson, H. L. 1966, *ARA&A*, 4, 193

- Johnson, J. A., Butler, R. P., Marcy, G. W., Fischer, D. A., Vogt, S. S., Wright, J. T., & Peek, K. M. G. 2007, *ApJ*, 670, 833
- Jones, H. R. A., et al. 2008, in *Society of Photo-Optical Instrumentation Engineers (SPIE) Conference Series*, Vol. 7014, Society of Photo-Optical Instrumentation Engineers (SPIE) Conference Series
- Jones, H. R. A., & Tsuji, T. 1997, *ApJ*, 480, L39
- Jurić, M., et al. 2008, *ApJ*, 673, 864
- Kaiser, N., et al. 2002, in *Survey and Other Telescope Technologies and Discoveries*. Edited by Tyson, J. Anthony; Wolff, Sidney. *Proc. of the SPIE*, Volume 4836, pp. 154-164 (2002)., 154–164
- Keller, S. C., et al. 2007, *Publications of the Astronomical Society of Australia*, 24, 1
- Kennedy, G. M., & Kenyon, S. J. 2008, *ApJ*, 673, 502
- Kirkpatrick, J. D. 2003, in *Proceedings of IAU Symposium 211: Brown Dwarfs*, ed. E. Martin, 189
- Kirkpatrick, J. D., Henry, T. J., & McCarthy, Jr., D. W. 1991, *ApJS*, 77, 417
- Kirkpatrick, J. D., Henry, T. J., & Simons, D. A. 1995, *AJ*, 109, 797
- Knapp, G. R., et al. 2004, *AJ*, 127, 3553
- Kornet, K., Wolf, S., & Różyczka, M. 2006, *A&A*, 458, 661
- Kovács, G., Zucker, S., & Mazeh, T. 2002, *A&A*, 391, 369
- Kuchner, M. J., & Lecar, M. 2002, *ApJ*, 574, L87
- Lacy, C. H. 1977, *ApJ*, 218, 444
- Laughlin, G., Bodenheimer, P., & Adams, F. C. 2004, *ApJ*, 612, L73
- Leggett, S. K., Allard, F., Dahn, C., Hauschildt, P. H., Kerr, T. H., & Rayner, J. 2000, *ApJ*, 535, 965
- Leggett, S. K., et al. 2002, *ApJ*, 564, 452
- Liu, M. C., Leggett, S. K., Golimowski, D. A., Chiu, K., Fan, X., Geballe, T. R., Schneider, D. P., & Brinkmann, J. 2006, *ApJ*, 647, 1393
- López-Morales, M. 2007, *ApJ*, 660, 732
- Maceroni, C., & Montalbán, J. 2004, *A&A*, 426, 577

- Mandel, K., & Agol, E. 2002, *ApJ*, 580, L171
- Marcy, G. W., Butler, R. P., Vogt, S. S., Fischer, D., & Lissauer, J. J. 1998, *ApJ*, 505, L147
- Maxted, P. F. L., & Jeffries, R. D. 2005, *MNRAS*, 362, L45
- McCullough, P. R., et al. 2006, *ApJ*, 648, 1228
- Metchev, S. A., Kirkpatrick, J. D., Berriman, G. B., & Looper, D. 2008, *ApJ*, 676, 1281
- Mountain, C. M., Selby, M. J., Leggett, S. K., Blackwell, D. E., & Petford, A. D. 1985, *A&A*, 151, 399
- Nutzman, P., & Charbonneau, D. 2008, *PASP*, 120, 317
- O’Donovan, F. T., et al. 2006, *ApJ*, 644, 1237
- Onaka, P., Tonry, J. L., Isani, S., Lee, A., Uyeshiro, R., Rae, C., Robertson, L., & Ching, G. 2008, in *Society of Photo-Optical Instrumentation Engineers (SPIE) Conference Series*, Vol. 7014, *Society of Photo-Optical Instrumentation Engineers (SPIE) Conference Series*
- Pickles, A. J. 1998, *PASP*, 110, 863
- Pinfield, D. J., et al. 2008, *MNRAS*, 390, 304
- Plavchan, P., Jura, M., Kirkpatrick, J. D., Cutri, R. M., & Gallagher, S. C. 2008, *ApJS*, 175, 191
- Pont, F., Bouchy, F., Melo, C., Santos, N. C., Mayor, M., Queloz, D., & Udry, S. 2005, *A&A*, 438, 1123
- Reid, I. N., Hawley, S. L., & Gizis, J. E. 1995, *AJ*, 110, 1838
- Reid, I. N., et al. 1999, *ApJ*, 521, 613
- . 2004, *AJ*, 128, 463
- Robin, A. C., Reyl e, C., Derri ere, S., & Picaud, S. 2003, *A&A*, 409, 523
- Rockenfeller, B., Bailer-Jones, C. A. L., Mundt, R., & Ibrahimov, M. A. 2006, *MNRAS*, 367, 407
- Sano, T., Miyama, S. M., Umebayashi, T., & Nakano, T. 2000, *ApJ*, 543, 486
- Schmidt-Kaler, T. 1982, *Landolt-B ornstein: Numerical Data and Functional Relationships in Science and Technology*, ed. K. Schaifers & H. H. Voigt (Springer-Verlag, Berlin), VI/2b
- Shaw, J. S., & L opez-Morales, M. 2007, in *Astronomical Society of the Pacific Conference Series*, Vol. 362, *The Seventh Pacific Rim Conference on Stellar Astrophysics*, ed. Y. W. Kang, H.-W. Lee, K.-C. Leung, & K.-S. Cheng, 15

- Siess, L., Dufour, E., & Forestini, M. 2000, *A&A*, 358, 593
- Stephens, D. C., & Leggett, S. K. 2004, *PASP*, 116, 9
- Stockton, A. 1999, *Ap&SS*, 269, 209
- Stone, J. M., Gammie, C. F., Balbus, S. A., & Hawley, J. F. 2000, *Protostars and Planets IV*, 589
- Torres, G. 2007, *ApJ*, 671, L65
- Tsuji, T., Ohnaka, K., Aoki, W., & Nakajima, T. 1996, *A&A*, 308, L29
- Tyson, J. A. 2002, in *Presented at the Society of Photo-Optical Instrumentation Engineers (SPIE) Conference, Vol. 4836, Society of Photo-Optical Instrumentation Engineers (SPIE) Conference Series*, ed. J. A. Tyson & S. Wolff, 10–20
- Welch, D. L., & Stetson, P. B. 1993, *AJ*, 105, 1813
- West, A. A., Hawley, S. L., Bochanski, J. J., Covey, K. R., Reid, I. N., Dhital, S., Hilton, E. J., & Masuda, M. 2008, *AJ*, 135, 785
- Zahn, J.-P. 1977, *A&A*, 57, 383

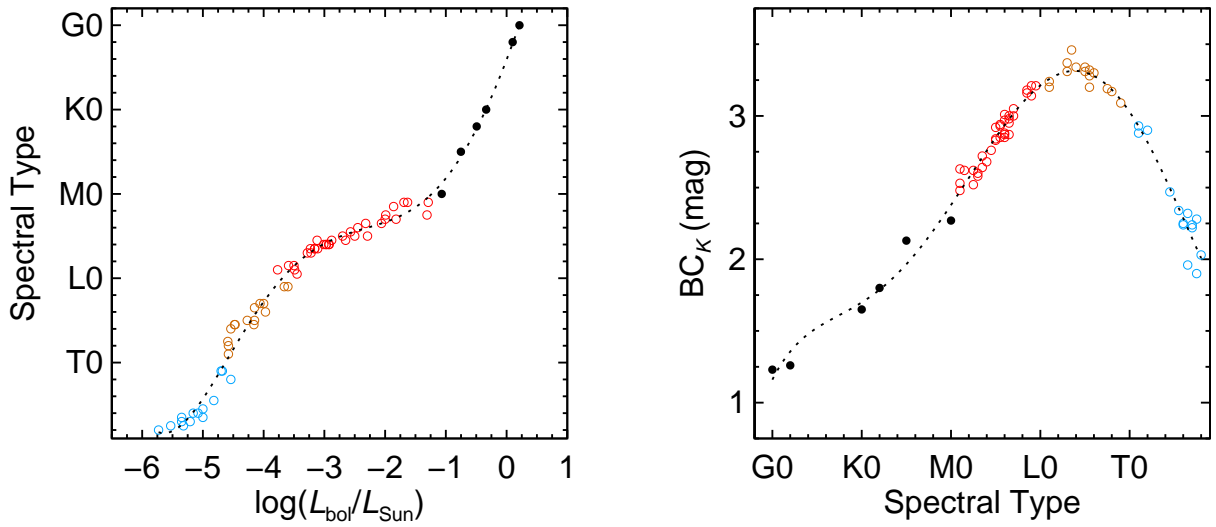


Fig. 1.— Empirical relations between spectral type, luminosity, and K -band bolometric correction. Open circles are objects with measured spectral types and luminosities, with M, L, and T dwarfs show in red, brown, and blue, respectively (Leggett et al. 2000, 2002; Golimowski et al. 2004). Filled black circles represent tabulated values from Cox (2000). The dotted lines show our fifth-order polynomial fits to these data, which we used to assign spectral types and BC_K values to objects in our simulations (see Table 2 for the coefficients).

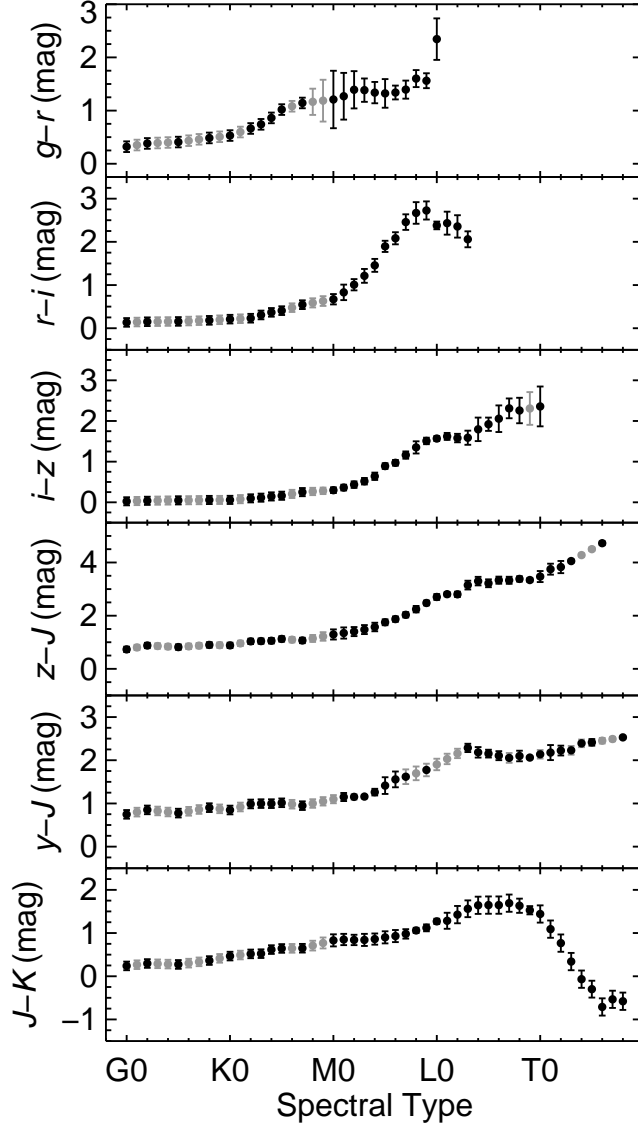


Fig. 2.— Optical and near-infrared colors of low-mass stars and brown dwarfs compiled from the literature or computed by us from synthetic photometry, as described in the Section 2.1. The filled circles and error bars represent the mean color at each spectral type and the rms. If fewer than 2 objects were available at a given spectral type, the mean was interpolated from the neighboring bin, likewise 3 objects were required for the rms. Gray symbols indicate spectral types where the mean and/or rms were interpolated. The color of each object in our simulation was drawn from a Gaussian distribution with a mean and rms appropriate for its spectral type.

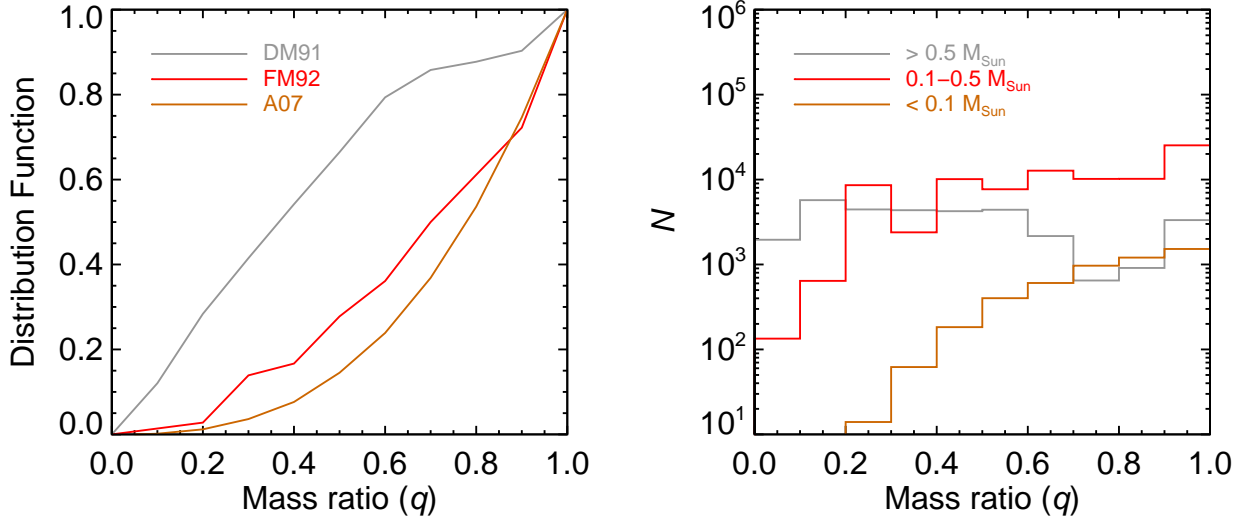


Fig. 3.— Mass ratio distribution of simulated binary companions in the PS1 3π Survey. We drew mass ratios from the cumulative distribution functions of objects from DM91 and FM92 for FGK stars ($> 0.5 M_{\odot}$) and early to mid-M dwarfs ($0.1\text{--}0.5 M_{\odot}$), respectively. For very low-mass stars and brown dwarfs ($< 0.1 M_{\odot}$), we used the power law of Allen (2007).

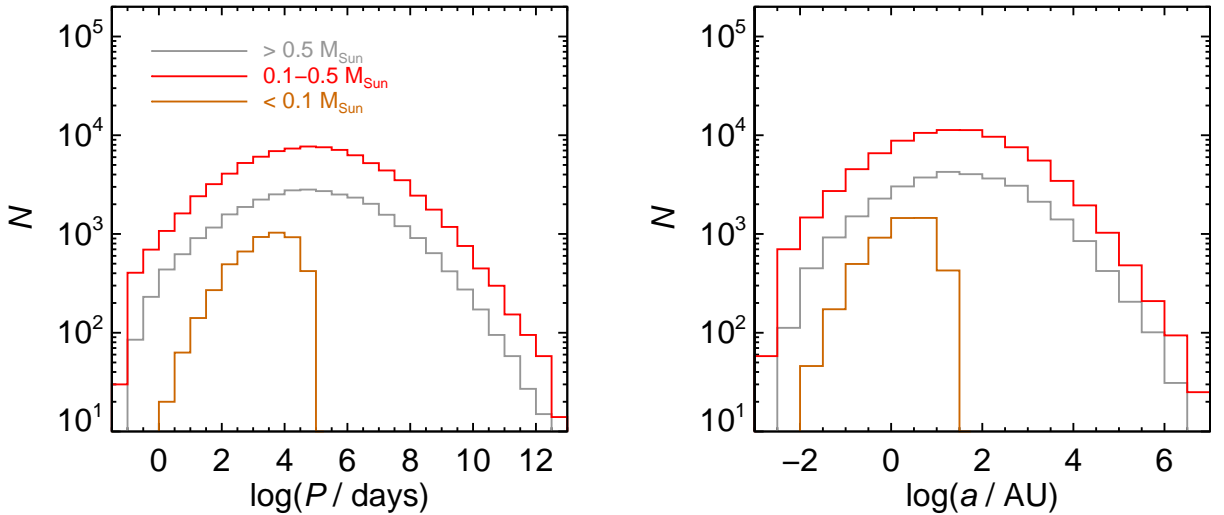


Fig. 4.— Orbital period and semimajor axis distributions of simulated binary companions in the PS1 3π Survey. For FGKM stars ($> 0.1 M_{\odot}$), we drew periods from the DM91 log-normal period distribution. For very low-mass stars and brown dwarfs ($< 0.1 M_{\odot}$), we drew periods from the log-normal period distribution of Basri & Reiners (2006), which is truncated at 15 AU. We converted period into semimajor axis using the system mass $M_1(1+q)$, where q is the mass ratio. The distributions appear truncated at short periods because 0.6% of companions were rejected on the basis of being non-detached.

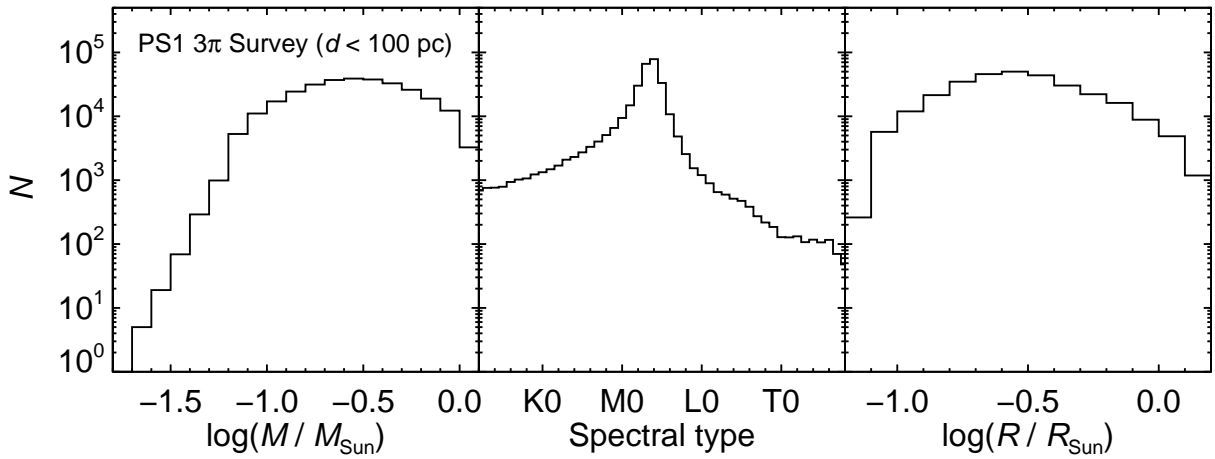


Fig. 5.— Predicted properties of objects detected in the PS1 3π Survey, restricted to stars within 100 pc for which PS1 will measure parallaxes. We have adopted the log-normal mass function of Covey et al. (2008), which appears truncated on the high mass end here due to the saturation limit of the 3π Survey. The spectral type distribution shows that, by far, the most common objects in this volume-limited sample are mid-M dwarfs. PS1 will also detect hundreds of T dwarfs and thousands of L dwarfs in the solar neighborhood. As a consequence of the preeminence of mid-M dwarfs, the typical radius in this sample is $\sim 0.3 R_{\odot}$. For such objects, transiting Jupiters would cause a $\sim 10\%$ flux diminution.

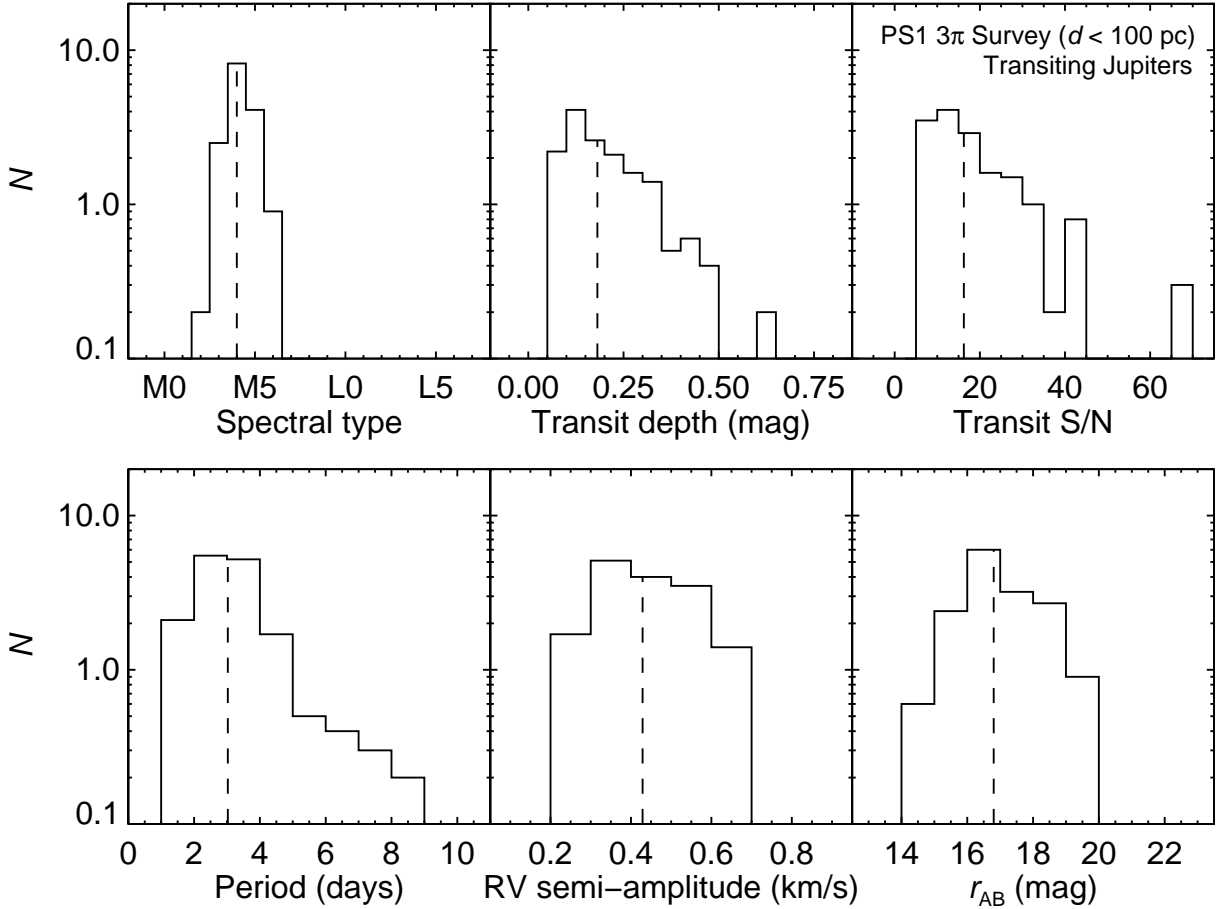


Fig. 6.— Properties of transiting Jupiter systems detected in our Monte Carlo simulations of the PS1 3π Survey, considering only stars within 100 pc. The dashed lines indicate the medians of the distributions. A total of 13 transiting systems are detected around mid-M dwarfs (M3–M5) exclusively, with large typical flux diminutions of 0.15 mag ($S/N_{\text{transit}} = 15$). The typical orbital period of 3 days for a $1 M_{\text{Jup}}$ planet results in a radial velocity semi-amplitude of 0.4 km s^{-1} . (Note that histograms have noninteger values because the simulation was oversampled by a factor of 10.)

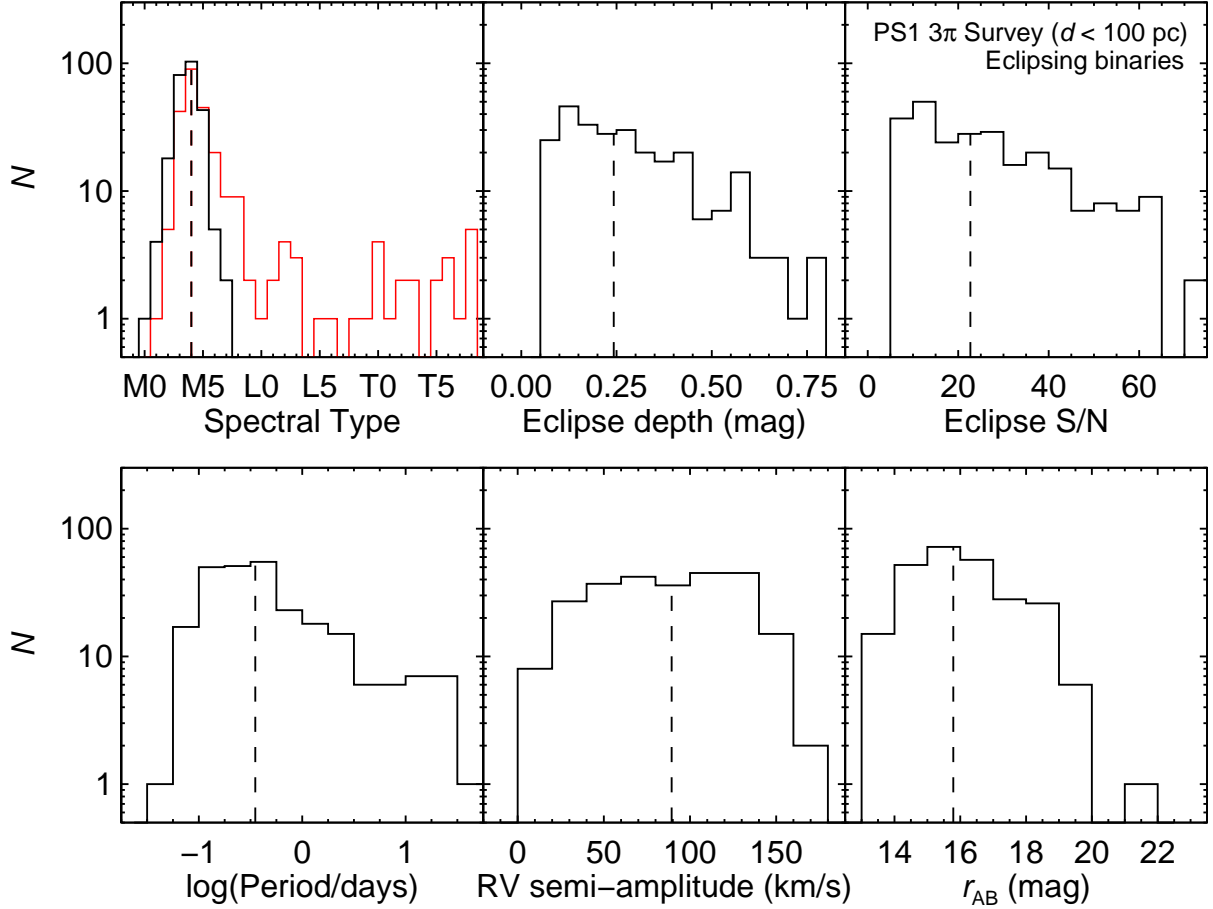


Fig. 7.— Properties of eclipsing binary systems detected in our Monte Carlo simulations of the PS1 3 π Survey, considering only stars within 100 pc. The dashed lines indicate the medians of the distributions. A total of 260 systems are detected, and the spectral types of the primaries are predominantly mid-M dwarfs (M3–M5, black line). The secondary components (red line) peak at a similar spectral type, but they extend to much later spectral types. Thus, ~ 10 late-M and ~ 10 L and T dwarfs are expected to be discovered in eclipsing binary systems by PS1, enabling the first direct measurements of the radii of field brown dwarfs. Typical detected eclipse depths are large (0.25 mag, $S/N_{\text{transit}} = 20$), and the integrated magnitudes are sufficiently bright ($r \approx 15.8$ mag) to measure precision radial velocities in the optical. The typical orbital period of 0.4 days results a large typical semi-amplitude of 80 km s^{-1} .

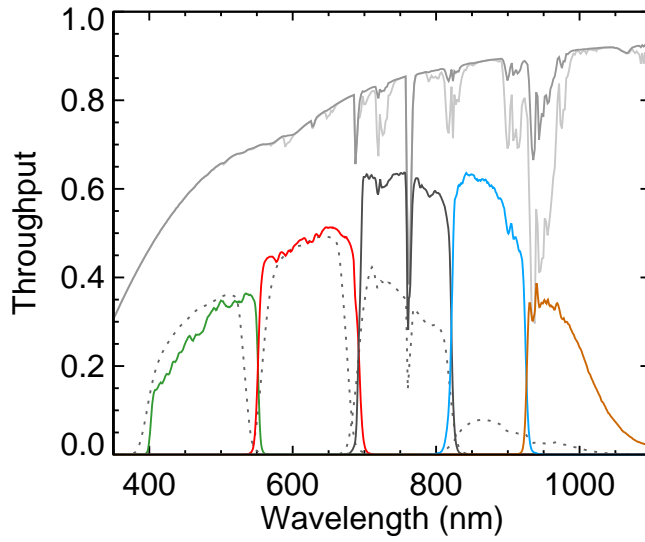


Fig. 8.— The total throughput of Pan-STARRS-1 bandpasses *g*, *r*, *i*, *z*, and *y* (green, red, dark gray, blue, and brown, respectively). For comparison, the SDSS bands are shown (dotted gray lines), with the primary differences being the absence of an SDSS *y* band, the longpass SDSS *z* band, and the greater overall red sensitivity of PS1 due to improved detector quantum efficiency at redder wavelengths. The atmospheric throughput at an airmass of 2 is also shown for 0.8 mm H₂O (darker gray) and 8 mm H₂O (lighter gray).

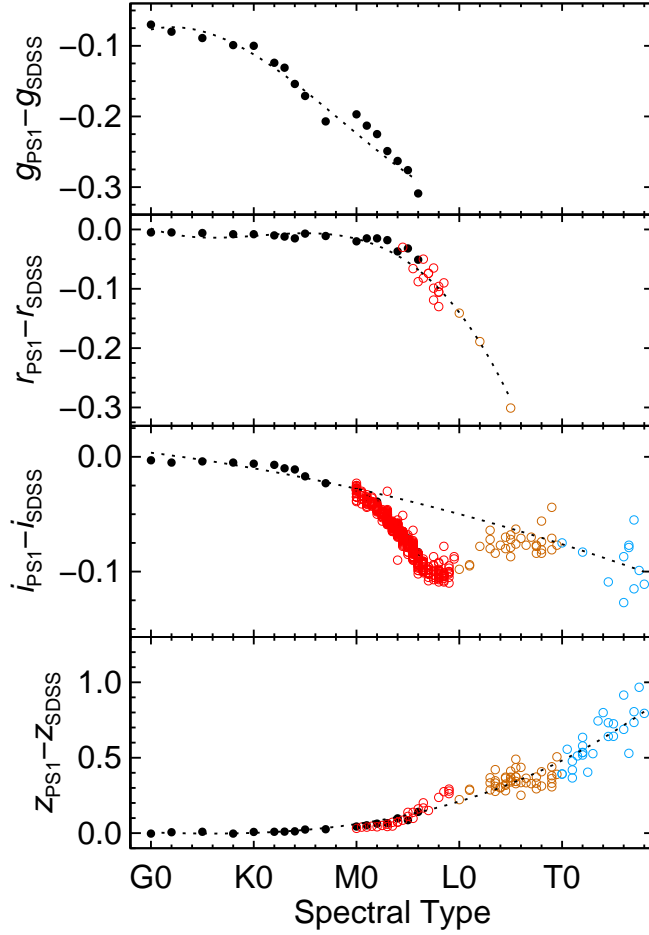


Fig. 9.— Conversions in magnitudes between the SDSS and PS1 photometric systems, derived from synthetic photometry as described in the text. Open circles indicate spectra of individual objects, with M, L, and T dwarfs show in red, brown, and blue, respectively. Filled black circles indicate the average stellar spectra of Pickles (1998). Polynomial fits to these data are shown by the dotted lines (coefficients are given in Table 6).

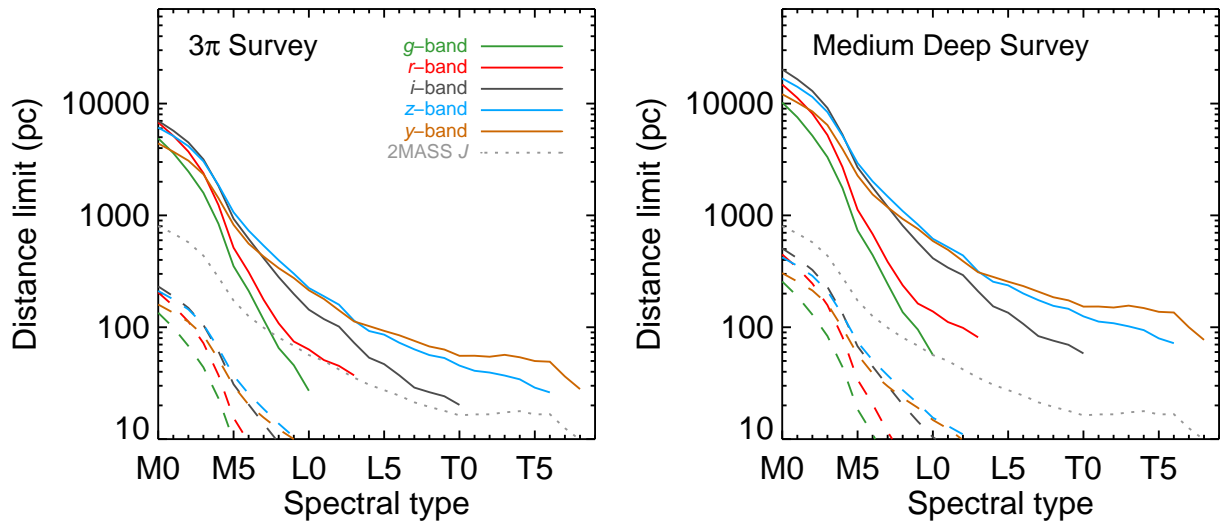


Fig. 10.— Distance at which objects of a given spectral type reach the survey detection limit ($S/N = 5$) in a given bandpass (solid lines). For comparison, the dotted line shows the detection limits for 2MASS ($J < 15.8$ mag). The dashed lines show the distances within which objects are expected to be saturated. The solid lines terminate at spectral types beyond which there is insufficient data to predict detection limits, as there is little published optical photometry or spectroscopy.

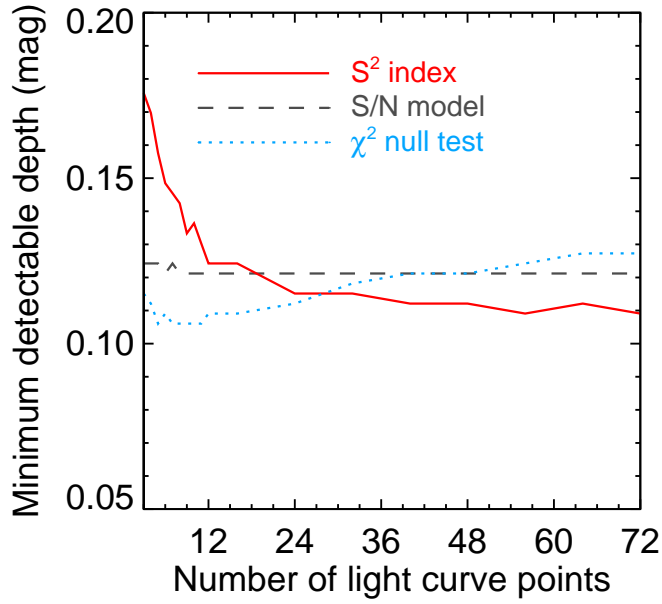


Fig. 11.— Minimum detectable eclipse depths for a source with $S/N = 100$ per epoch using the algorithms described in the text, adopting an eclipse threshold S/N of 7. The S^2 index (solid line, Bramich et al. 2008) improves significantly as more light curve points are added. The S/N model (dashed line) does not improve because we have assumed a photometric floor at $S/N = 100$, so adding more light curve points does not reduce the noise in this example. The χ^2 null test (dotted line) becomes less sensitive with the number of light curve points, since adding more constant flux points reduces the significance of the single discrepant point.

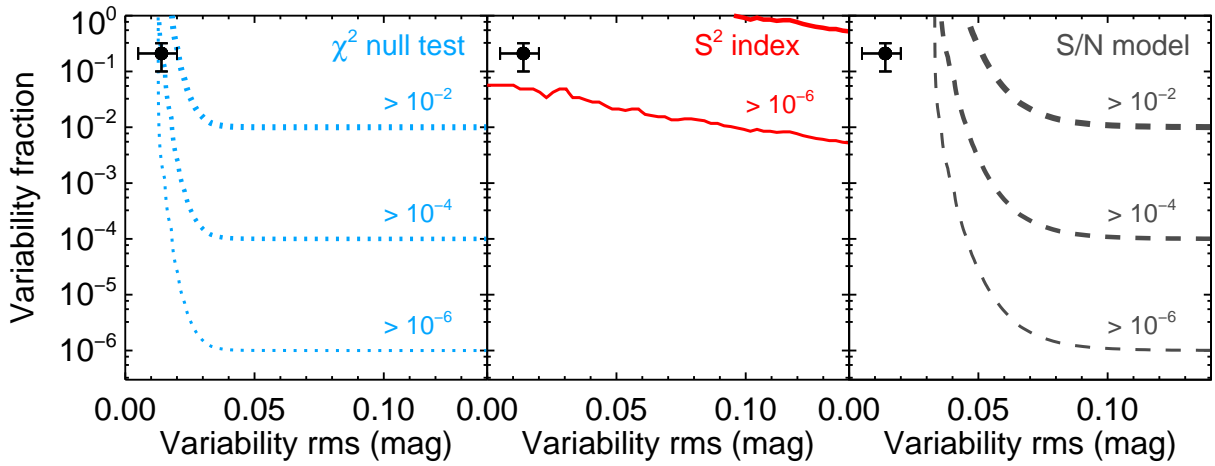


Fig. 12.— Contours of the false positive rate due to star spots for the three eclipse detection algorithms described in the text. Contours are drawn at false positive rates of 10^{-2} , 10^{-4} , and 10^{-6} , adopting an eclipse threshold S/N of 7. We modeled star spots as sinusoidal variability with over a range amplitudes ($0.0 < \text{rms} < 0.14$ mag). As a point of comparison, the best available estimate of variability among M dwarfs from Rockenfeller et al. (2006) is shown as a filled circle with errors. The χ^2 null test (dotted line) is the most vulnerable to contamination from star spots, while the S^2 index (solid line) and S/N model (dashed line) are vulnerable to more limited, different source populations of false positives: rare, highly variable objects for the S/N model and common objects with a low level of variability for the S^2 index.

Table 1. Model of Extended Solar Neighborhood ($d < 100$ pc)

Spectral Type	$N_{\text{all}}^{\text{a}}$	PS1 3π (saturated) ^b
Stars and brown dwarfs		
Total	4.0×10^5	2.1×10^5 (8.5×10^4)
G+K dwarfs	5.2×10^4	0 (3.9×10^4)
M dwarfs	3.4×10^5	2.1×10^5 (4.6×10^4)
L dwarfs	8000	5400 (0)
T dwarfs	6900	880 (0)
Transiting Jupiter hosts ^c		
Total	142	57 (47)
G+K dwarfs	44	0 (33)
M dwarfs	94	56 (14)
L+T dwarfs	4	1 (0)
Eclipsing binary primaries ^c		
Total	1284	573 (400)
G+K dwarfs	280	0 (210)
M dwarfs	1000	570 (190)
L+T dwarfs	4	3 (0)

^aAll objects within 100 pc.

^bNumber of sources within the magnitude limits of (saturated in) the Pan-STARRS 3π Survey.

^cNumber of systems with orbits aligned such that transits/eclipses are allowed, but not necessarily detected by the PS1 3π Survey. These numbers reflect how many such systems are within the magnitude limits of the 3π Survey.

Table 2. Empirical Spectral Type Relations

Poly. fit	SpT – L_{bol}	BC_K – SpT
c_0	-1.5917×10^1	2.3785
c_1	-1.8829×10^1	9.3034×10^{-2}
c_2	-3.9862	1.2667×10^{-3}
c_3	1.3840	-1.9272×10^{-4}
c_4	6.6571×10^{-1}	-4.9479×10^{-6}
c_5	6.3156×10^{-2}	1.9198×10^{-7}
rms	1.1	0.08

References. — Polynomial fits are valid between spectral types G0 and T8, where

$$\text{SpT} = \sum_{i=0}^5 c_i \times \log(L_{\text{bol}}/L_{\odot})^i$$

$$\text{BC}_K = \sum_{i=0}^5 c_i \times \text{SpT}^i$$

Numerical spectral types are defined as (G0, K0, M0, L0, T0) = (–20, –10, 0, 10, 20).

Table 3. Optical and Near-infrared Colors of Low-Mass Stars and Brown Dwarfs^a

SpT	$g - r$	$r - i$	$i - z$	$z - J$	$y - J$	$J - K$
G0	0.32±0.10	0.14±0.10	0.02±0.10	0.73±0.10	0.75±0.10	0.24±0.10
G1	0.35±0.10 ^b	0.14±0.10 ^b	0.03±0.10 ^b	0.81±0.10 ^b	0.80±0.10 ^b	0.27±0.10 ^b
G2	0.38±0.10	0.15±0.10	0.04±0.10	0.88±0.10	0.85±0.10	0.30±0.10
G3	0.39±0.10 ^b	0.15±0.10 ^b	0.04±0.10 ^b	0.86±0.10 ^b	0.83±0.10 ^b	0.29±0.10 ^b
G4	0.40±0.10 ^b	0.16±0.10 ^b	0.04±0.10 ^b	0.84±0.10 ^b	0.80±0.10 ^b	0.28±0.10 ^b
G5	0.41±0.10	0.16±0.10	0.05±0.10	0.82±0.10	0.78±0.10	0.27±0.10
G6	0.43±0.10 ^b	0.17±0.10 ^b	0.05±0.10 ^b	0.85±0.10 ^b	0.82±0.10 ^b	0.30±0.10 ^b
G7	0.46±0.10 ^b	0.17±0.10 ^b	0.05±0.10 ^b	0.87±0.10 ^b	0.86±0.10 ^b	0.33±0.10 ^b
G8	0.49±0.10	0.18±0.10	0.06±0.10	0.90±0.10	0.90±0.10	0.36±0.10
G9	0.51±0.10 ^b	0.20±0.10 ^b	0.06±0.10 ^b	0.89±0.10 ^b	0.88±0.10 ^b	0.41±0.10 ^b
K0	0.53±0.10	0.21±0.10	0.06±0.10	0.88±0.10	0.85±0.10	0.47±0.10
K1	0.60±0.10 ^b	0.22±0.10 ^b	0.08±0.10 ^b	0.96±0.10 ^b	0.92±0.10 ^b	0.49±0.10 ^b
K2	0.66±0.10	0.23±0.10	0.10±0.10	1.03±0.10	0.99±0.10	0.52±0.10
K3	0.74±0.10	0.31±0.10	0.11±0.10	1.04±0.10	1.00±0.10	0.52±0.10
K4	0.86±0.10	0.37±0.10	0.15±0.10	1.06±0.10	1.00±0.10	0.62±0.10
K5	1.02±0.10	0.41±0.10	0.16±0.10	1.12±0.10	1.02±0.10	0.64±0.10
K6	1.08±0.10 ^b	0.48±0.10 ^b	0.21±0.10 ^b	1.10±0.10 ^b	0.98±0.10 ^b	0.65±0.10 ^b
K7	1.14±0.10	0.55±0.10	0.25±0.10	1.07±0.10	0.95±0.10	0.65±0.10
K8	1.16±0.25 ^b	0.59±0.11 ^b	0.27±0.09 ^b	1.14±0.13 ^b	1.00±0.10 ^b	0.71±0.11 ^b
K9	1.19±0.39 ^b	0.63±0.11 ^b	0.28±0.08 ^b	1.22±0.16 ^b	1.05±0.10 ^b	0.77±0.13 ^b
M0	1.21±0.54	0.67±0.12	0.30±0.07	1.29±0.19	1.10±0.10 ^b	0.83±0.14
M1	1.27±0.44	0.83±0.18	0.36±0.07	1.35±0.21	1.15±0.09	0.85±0.13
M2	1.39±0.35	1.01±0.13	0.44±0.08	1.40±0.17	1.15±0.07 ^c	0.84±0.12
M3	1.38±0.22	1.21±0.16	0.52±0.08	1.48±0.17	1.16±0.04	0.84±0.14
M4	1.34±0.20	1.46±0.15	0.64±0.09	1.57±0.16	1.26±0.08	0.86±0.13
M5	1.32±0.27	1.90±0.13	0.89±0.07	1.75±0.11	1.41±0.19	0.90±0.14
M6	1.34±0.13	2.08±0.14	0.97±0.07	1.87±0.10	1.56±0.18	0.93±0.14
M7	1.39±0.17	2.46±0.18	1.16±0.09	2.03±0.10	1.62±0.17 ^c	0.98±0.11
M8	1.60±0.16	2.67±0.25	1.35±0.15	2.24±0.12	1.70±0.16 ^b	1.06±0.06
M9	1.56±0.14	2.73±0.21	1.51±0.08	2.48±0.09	1.77±0.15 ^c	1.12±0.08
L0	2.34±0.39	2.38±0.09	1.57±0.06	2.70±0.11	1.90±0.13 ^b	1.27±0.06
L1	...	2.43±0.27	1.62±0.09	2.81±0.08	2.03±0.12 ^b	1.28±0.19
L2	...	2.36±0.26	1.58±0.10	2.80±0.10	2.16±0.11 ^b	1.43±0.20

Table 3—Continued

SpT	$g - r$	$r - i$	$i - z$	$z - J$	$y - J$	$J - K$
L3	...	2.06 ± 0.18	1.59 ± 0.17	3.15 ± 0.16	2.29 ± 0.10	1.56 ± 0.19
L4	1.79 ± 0.29	3.30 ± 0.16	2.18 ± 0.12	1.64 ± 0.20
L5	1.92 ± 0.16	3.22 ± 0.15	2.15 ± 0.09	1.65 ± 0.20
L6	2.06 ± 0.33	3.34 ± 0.13	2.11 ± 0.10	1.65 ± 0.20
L7	2.31 ± 0.24	3.33 ± 0.13	2.05 ± 0.11^c	1.69 ± 0.20
L8	2.26 ± 0.31	3.38 ± 0.10	2.10 ± 0.12	1.63 ± 0.17
L9	2.31 ± 0.40^b	3.34 ± 0.07	2.06 ± 0.02	1.53 ± 0.09
T0	2.36 ± 0.49	3.47 ± 0.21	2.14 ± 0.10^c	1.44 ± 0.20
T1	3.75 ± 0.21	2.18 ± 0.17	1.09 ± 0.20
T2	3.83 ± 0.23	2.22 ± 0.11	0.77 ± 0.20
T3	4.05 ± 0.06	2.23 ± 0.10^c	0.34 ± 0.20
T4	4.28 ± 0.06^b	2.39 ± 0.09^c	-0.07 ± 0.20
T5	4.50 ± 0.06^b	2.41 ± 0.08	-0.30 ± 0.19
T6	4.73 ± 0.07	2.45 ± 0.06^b	-0.71 ± 0.20
T7	2.49 ± 0.05^b	-0.53 ± 0.20
T8	2.53 ± 0.04^c	-0.58 ± 0.20

^aOptical photometry (*grizy*) on the PS1 system in AB magnitudes. Near-infrared photometry (*JK*) on the MKO system in Vega magnitudes.

^bMean and rms are interpolated from neighboring spectral type bins.

^cOnly the rms is interpolated from neighboring spectral type bins.

References. — Pickles (1998); Hawley et al. (2002); Knapp et al. (2004); Stephens & Leggett (2004); Chiu et al. (2006); Bochanski et al. (2007); West et al. (2008); Faherty et al. (2009)

Table 4. PS1 3π Simulation Results for Number of Eclipsing Systems

Survey Yield	Bandpass					Total (F.P.) ^a
	<i>g</i>	<i>r</i>	<i>i</i>	<i>z</i>	<i>y</i>	
	Semi-analytic					
Transiting Jupiters	3.7	3.5	2.8	2.6	3.3	15.9 ^b
	Monte Carlo					
Transiting Jupiters	3.4	3.5	2.9	2.8	3.4	12.6 ^c (0.0)
Eclipsing binaries	160	140	80	90	110	260 ^c (0)

^aNumber of false positives is given in parentheses.

^bThis total does not account for double counting caused by transits detected in multiple bandpasses around the same star.

^cThis total counts transits detected in multiple bandpasses for the same star only once, and thus is not simply the sum of the number of detections in individual bandpasses.

Table 5. AB Zero-Magnitude Properties of PS1 Bandpasses

Band	$\lambda_{\text{eff},0}^{\text{a}}$ μm	Φ_0^{b} $\text{DN s}^{-1} \text{ m}^{-2}$	$F_{\lambda,0}^{\text{a}}$ $\text{W m}^{-2} \mu\text{m}^{-1}$	$\Phi_{\text{sky}}^{\text{c}}$ $\text{DN s}^{-1} \text{ m}^{-2} \text{ ''}^{-2}$	$\Delta_{\text{Vega}}^{\text{d}}$ mag
<i>g</i>	0.484	4.73×10^9	4.75×10^{-8}	6.9	0.08
<i>r</i>	0.621	5.87×10^9	2.86×10^{-8}	22.5	−0.16
<i>i</i>	0.754	5.55×10^9	1.93×10^{-8}	48.7	−0.38
<i>z</i>	0.869	3.78×10^9	1.45×10^{-8}	77.6	−0.54
<i>y</i>	0.979	1.85×10^9	1.14×10^{-8}	89.6	−0.62

^aEffective wavelength ($\lambda_{\text{eff},0}$) and effective flux density ($F_{\lambda,0}$) in each bandpass for a zero-magnitude source. Computed by integrating the wavelength and flux density weighted by the transmission curve of the bandpass, $T(\lambda)$, and the photon flux density of the zero-magnitude source, $F_{\lambda,0}(\lambda)/(hc/\lambda)$.

^bTotal integrated photon flux of the zero-magnitude source in each bandpass.

^cSky brightness derived from synthetic photometry of the Mauna Kea airglow spectrum obtained by Stockton (1999) using Keck/LRIS. This sky spectrum terminates at 1.04 μm , and since 8% of the area of the *y* band lies beyond 1.04 μm , the sky flux in this band is likely underestimated.

^dAB to Vega conversions ($\Delta_{\text{Vega}} \equiv m_{\text{Vega}} - m_{\text{AB}}$) derived from synthetic photometry of a flux-calibrated spectrum of Vega (Hayes 1985; Mountain et al. 1985).

Table 6. SDSS to PS1 Photometric System Conversions

Poly. fit	$g_{\text{PS1}} - g_{\text{SDSS}}$	$r_{\text{PS1}} - r_{\text{SDSS}}$	$i_{\text{PS1}} - i_{\text{SDSS}}$	$z_{\text{PS1}} - z_{\text{SDSS}}$
c_0	-2.2409×10^{-1}	-1.5839×10^{-2}	-2.7831×10^{-2}	6.0387×10^{-2}
c_1	-1.2085×10^{-2}	-4.3486×10^{-3}	-1.9926×10^{-3}	9.9246×10^{-3}
c_2	5.6155×10^{-5}	-5.9648×10^{-4}	-2.1100×10^{-5}	4.5737×10^{-4}
c_3	1.4624×10^{-5}	-2.1129×10^{-5}	...	4.9887×10^{-6}

References. — Polynomial fits are a function of spectral type (SpT), where

$$\text{mag}(\text{PS1}) - \text{mag}(\text{SDSS}) = \sum_{i=0}^5 c_i \times (\text{SpT})^i$$

and numerical spectral types are defined as (G0, K0, M0, L0, T0) = (−20, −10, 0, 10, 20). Fits are valid from G0 to T8 for i and z bands, from G0 to L5 for r band, and from G0 to M6 for g band.

Table 7. Pan-STARRS-1 3π Survey

Band	N_{epoch}	t_{exp} (s)	$m_{\text{lim}}^{\text{a}}$ (mag)	$m_{\text{floor}}^{\text{b}}$ (mag)	$m_{\text{sat}}^{\text{c}}$ (mag)	$\text{SpT}_{\text{sat}}^{\text{d}}$
<i>g</i>	12	60	23.4	18.7	15.6	M1
<i>r</i>	12	38	22.8	18.3	15.3	M2
<i>i</i>	12	30	22.2	17.9	14.8	M3
<i>z</i>	12	30	21.6	17.4	14.4	M3
<i>y</i>	12	30	20.1	15.9	12.8	M2

^aFaintest magnitude that has a S/N of 5.

^bFaintest magnitude that has a S/N of $S/N_{\text{floor}} = 100$.

^cSaturation limits derived for a Gaussian PSF with a FWHM of $0''.8$, a gain of $1 e^- \text{ DN}^{-1}$, a full-well depth of $3.0 \times 10^4 e^-$.

^dEarliest spectral type that is not saturated at 100 pc.

Table 8. Pan-STARRS-1 Medium Deep Survey

Band	N_{epoch}	$N \times t_{\text{exp}}$ (s)	$m_{\text{lim}}^{\text{a}}$ (mag)	$m_{\text{floor}}^{\text{b}}$ (mag)	$m_{\text{sat}}^{\text{c}}$ (mag)	SpT _{sat} ^d
<i>g</i>	72	3×240	24.8	20.9	16.8	M3
<i>r</i>	72	3×240	24.4	20.8	16.8	M4
<i>i</i>	72	6×240	24.4	20.9	16.4	M5
<i>z</i>	72	6×240	23.7	20.3	15.7	M4
<i>y</i>	72	6×240	22.8	19.4	14.8	M4

^aFaintest magnitude that has a S/N of 5.

^bFaintest magnitude that has a S/N of $S/N_{\text{floor}} = 100$.

^cSaturation limits derived for a Gaussian PSF with a FWHM of $0''.8$, a gain of $1 e^- \text{ DN}^{-1}$, a full-well depth of $3.0 \times 10^4 e^-$.

^dEarliest spectral type that is not saturated at 100 pc.